Oil & Natural Gas Technology

DOE Award No.: DE-FE0024297

Quarterly Research Performance

Progress Report (Period Ending 12/31/2017)

Marcellus Shale Energy and Environment Laboratory (MSEEL)

Project Period (October 1, 2014 – September 30, 2019)

Submitted by:
Samuel Taylor

Signature

West Virginia University Research Corporation
DUN's Number: 191510239
886 Chestnut Ridge Road,
PO Box 6845, Morgantown WV, 26505
Tim.Carr@mail.wvu.edu
304-293-9660

Prepared for:
United States Department of Energy
National Energy Technology Laboratory

1/31/2018

U.S. DEPARTMENT OF ENERGY | NATIONAL ENERGY TECHNOLOGY LABORATORY

Office of Fossil Energy

Executive Summary

The objective of the Marcellus Shale Energy and Environment Laboratory (MSEEL) is to provide a long-term field site to develop and validate new knowledge and technology to improve recovery efficiency and minimize environmental implications of unconventional resource development.

This quarter field work focused on integration of subsurface data including fiber-optic Distributed Acoustic Sensing (DAS) and Distributed Temperature Sensing (DTS) data with microseismic and borehole data to better understand reservoir behavior. In addition all data generated by MSEEL was moved to a publically available website.

All MSEEL material and results from all topics were summarized at an External Project Review on 5 December, 2017.

Numerous papers and presentations and two patent discoveries highlight the rapid integration and the significant results beginning to appear from the MSEEL project.

Quarterly Progress Report

October 1 – December 31, 2017

Project Performance

This report summarizes the activities of Cooperative Agreement DE-FE0024297 (Marcellus Shale Energy and Environment Laboratory – MSEEL) with the West Virginia University Research Corporation (WVURC) during the first quarter of FY2018 (October 1 through December 31, 2017).

This report outlines the approach taken, including specific actions by subtopic. If there was no identified activity during the reporting period, the appropriate section is included but without additional information.

A summary of major lessons learned to this point of the project are provided as bullet points and will be added to as research is completed. New lessons are listed below.

1) Marcellus fractures result in cross-flow between stages and reduced completion efficiency that appears to affect production efficiency.
2) The cross-flow can be detected using advanced seismic attributes applied to fiber-optic DAS data. This is the first instance of using this approach with DAS data and has resulted in the development of software and a patent discovery.
3) Geochemical data is providing insight into the structure and chemistry of kerogen in the Marcellus and its interaction with completion fluids.

Project Management Update

Approach

The project management team will work to generate timely and accurate reporting, and to maintain project operations, including contracting, reporting, meeting organization, and general oversight.

Results and Discussion

The project team is tracking eight (8) milestones in this budget period.

3/1/2017 - Completed Production Logging (Scheduled 2/15/2017; Completed 3/15/2017)
4/30/17 - Conduct preliminary analysis of production log data and present to DOE (Underway)
8/15/17 - Coordinate and hold MSEEL session at URTEC 2017
8/30/17 - Complete rock geochemistry and geomechanical data analysis and integration with log & microseismic data to develop preliminary reservoir simulation and fracture model(s)
8/30/17 – Create a comprehensive online library of MSEEL presentations and papers that can be downloaded. Maintain with additional material through end of project.
8/30/17 – Reorganize MSEEL data portal and prepare to transfer to NETL for public dissemination.
12/31/17 – Complete a detailed reservoir simulation incorporating fracture geometry and flow simulation
12/31/17 - Determine changes in kerogen structure and bulk rock interactions and composition on interaction with fracturing fluids under simulated subsurface conditions.

Topic 1 – Geologic Engineering

Approach

We presented several papers showing the importance of multidisciplinary and multi-institutional team undertaking integrated geoscience, engineering and environmental studies to develop new knowledge of subsurface geology and engineering, and surface environmental impact to identify best practices that can optimize hydraulic fracture stimulation to increase flow rates, estimated ultimate recovery in order to reduce the number of wells and environmental impact.

Results and Discussion

The permeability measurement experiments for additional core plugs from the science are continuing. The measured permeability values are in the same range as ones previously measured. The measurement results indicated that the flow regime is transition flow for pore pressures below 900 psia and it is slip flow for pore pressure above 1000 psia.

The modified Klinkenberg correction is necessary when the flow regime is transition flow while Klinkenberg correction is sufficient under the slip flow conditions.

We used several techniques to characterize the pore microstructure, porosity, mineralogy and elemental composition of the Mahantango Formation and Marcellus using a combination of focus ion beam (FIB) scanning electron microscope (SEM), X-ray fluorescence (XRF) and low-pressure nitrogen adsorption methods on core samples acquired from three wells in West Virginia. We have developed advanced image processing software to analyze the pore size, organic matter (OM), OM porosity, and porosity developed in inorganic rock matrix (patent discovery in preparation). There is a significant amount of porosity beyond the resolution of SEM. BET, t-Plot, H-K, and BJH models were used to interpret the isotherms of nitrogen-adsorption test, and distinguished specific surface areas (SSA), pore volumes, proportions or micropores and mesopores, and pore-size distributions (pore width down to 2nm) of core samples, which helped explaining the fact that SEM technology underestimated the porosity values compare to helium porosimeter. The results were presented at a SEPM – AAPG Hedberg Research Conference.

Presentations

1) Song, Liaosha and **Timothy R. Carr**, Microstructural Evolution of Organic Matter Pores in Middle Devonian Black Shale from West Virginia and Pennsylvania, USA, SEPM – AAPG Hedberg Research Conference, Mudstone Diagenesis, Santa Fe, New Mexico, October 16-19. http://www.searchanddiscovery.com/pdfz/abstracts/pdf/2017/90283hedberg/abstracts/ndx_song.pdf.html
2) **Carr, Timothy R.**, The Importance of Field Demonstration Sites: The View from the Unconventional Resource Region of the Appalachian Basin (Invited), [H21K-06] presented at 2017 Fall Meeting, AGU, New Orleans, LA, 11-15 Dec. https://agu.confex.com/agu/fm17/meetingapp.cgi/Paper/242523

Plan for Next Quarter

Finish patent discovery and work to further characterize pore structure in the Marcellus. Integrate with results from Topic 3: Deep Subsurface Rock, Fluids and Gas.

Topic 2 – Geophysical & Geomechanical

Approach

During this quarterly period, the influence of a discrete fracture network on the growth of hydraulic fractures was investigated through the use of numerical modeling. The model described in a previous quarterly report was used to compute hydraulic fracture dimensions for stage 21 through stage 28 of well MIP 3H. We also investigated seismic attribute techniques to analysis of fiber-optic Distributed Acoustic Sensing (DAS) data and integrate with Distributed Temperature Sensing (DTS) data and microseismic. Results reveal the presence of cross-flow between stages.

Results & Discussion

Geophysical

Paper noted last quarter is in-press. The following paper is available online and in paper from *Interpretation,* ***6,*** *2 (May 2018).*

Marcellus Shale model stimulation tests and microseismic response yield insights into mechanical properties and the reservoir DFN. Interpretation. 50p. published December 4, 2017, Interpretation, Society Exploration Geophysicists https://doi.org/10.1190/int-2016-0199.1

Thomas H. Wilson , **Tim Carr** , B. J. Carney , Malcolm Yates , Keith MacPhail , Adrian Morales , Ian Costello , Jay Hewitt , Emily Jordon , Natalie Uschner , Miranda Thomas , Si Akin , Oluwaseun Magbagbeola , Asbjoern Johansen , Leah Hogarth , Olatunbosun Anifowoshe , and Kashif Naseem,

Abstract

We present stimulation tests of a model discrete fracture network (DFN) in the Marcellus Shale reservoir near Morgantown, West Virginia. The microseismic response observed on the modeled stage is characteristic of that observed in several stages along the length of the horizontal well so that the workflow developed in this paper can be easily extended to other stages in this and other Marcellus Shale wells. The model DFN is designed using log data, including fracture image logs from vertical pilot and horizontal wells. Data from these wells provide geomechanical properties, fracture trend and intensity and stress orientation. Microseismic cluster trends provide additional constraints on geomechanical model development. Results from stimulation tests are used to modify the reservoir DFN and geomechanical model. Modifications ensure consistency with borehole observations. Fractures observed along the length of the horizontal well consist

predominantly of one set, while two sets are observed in the vertical pilot well. These two sets are required in the model DFN to reproduce the stimulation trend inferred from microseismic data. Northeast asymmetry in the microseismicity associated with hydraulic fracture treatment is interpreted to result from a horizontal drop of Shmin toward a previously drilled well. The asymmetry is interpreted to result from stress reduction associated with treatment of an earlier parallel well, presence of a cross-strike structure parallel to the well or a combination of the two. Limited downward growth, inferred from the microseismic response, required increase of the minimum stress in model strata underlying the Marcellus.

Read More: https://library.seg.org/doi/10.1190/int-2016-0199.1

We worked to develop techniques to process fiber-optic DAS data using seismic attribute approaches. This resulted in submission of a patent discover and a paper on application of seismic attributes for processing, which was presented at the SPE Hydraulic Fracturing Technology Conference and Exhibition. The paper included as Appendix 1 was the most downloaded paper from OnePetro for the last 30 days (Figure 2.0). Title is:

Ghahfarokhi, P. K., Carr, T., Song, L., Shukla, P., & Pankaj, P. (2018, January 23). Seismic Attributes Application for the Distributed Acoustic Sensing Data for the Marcellus Shale: New Insights to Cross-Stage Flow Communication. Society of Petroleum Engineers, doi:10.2118/189888-MS.

We also presented two papers at the American Geophysical Union Annual meeting on geophysical responses to hydraulic fracture stimulation. One of which was invited for publication in an upcoming book.

1) Kavousi, Payam, **Timothy R**. **Carr,** Robert J Mellors, Improved interpretation of Distributed Acoustic Sensing (DAS) fiber optic data in stimulated wells using seismic attributes, [S33B-0865] presented at December 2017 Fall Meeting, AGU, New Orleans, LA, 11-15,https://agu.confex.com/agu/fm17/meetingapp.cgi/Paper/282093
2) Mellors Robert J, Christopher Scott Sherman, Frederick J Ryerson, Joseph Morris, Graham S Allen, Michael J Messerly, **Timothy Carr**, Payam Kavousi, Modeling borehole microseismic and strain signals measured by a distributed fiber optic sensor, [S33B-0869] presented at 2017 Fall Meeting, AGU, New Orleans, LA, 11-15, https://agu.confex.com/agu/fm17/meetingapp.cgi/Paper/264800

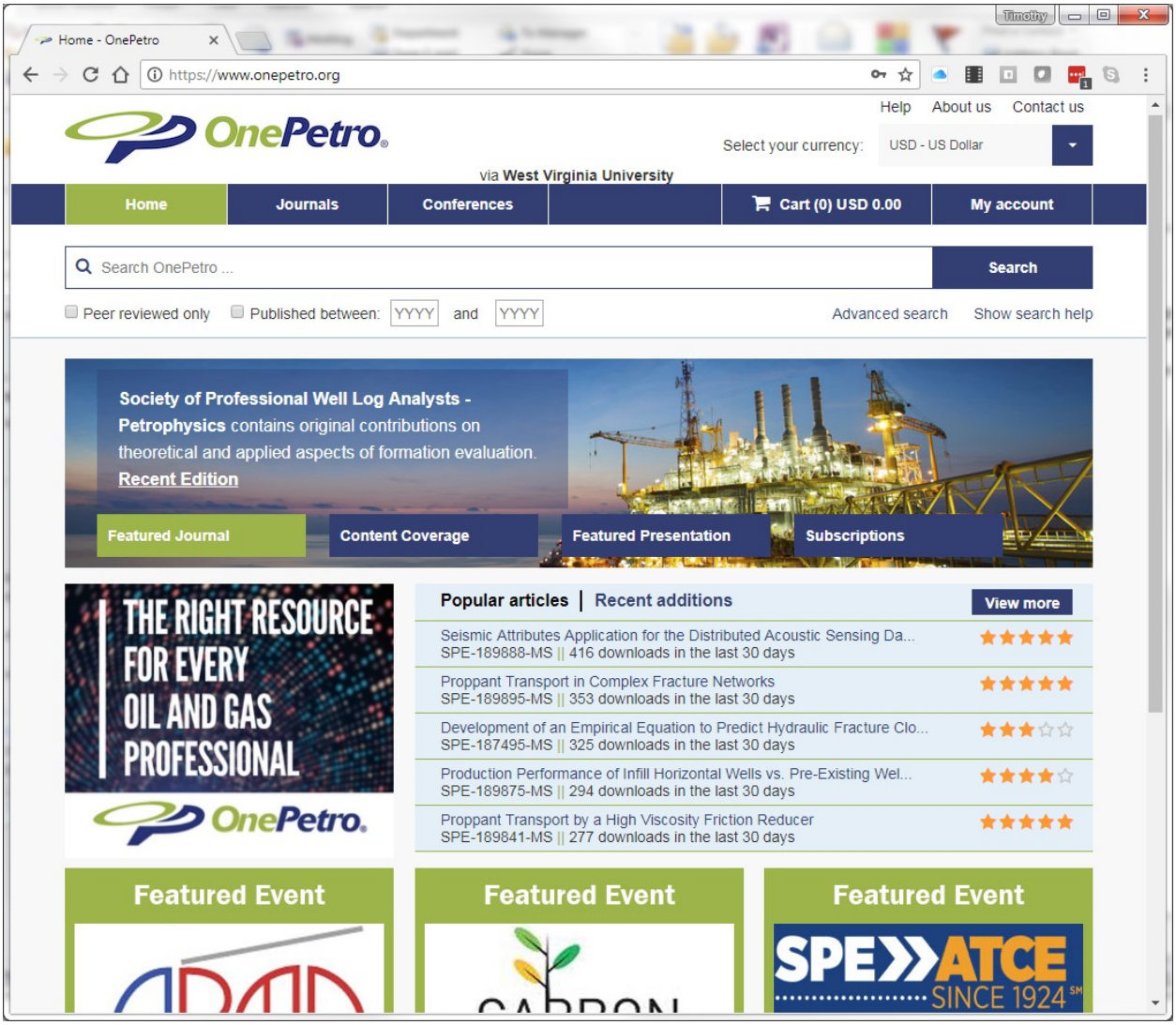

Figure 2.0 - Screen Shot of OnePetro web site on 1/30/18, showing that SPE-189888-MS continues to be the most downloaded paper and rank five stars.

Geomechanical

Table 2.1 shows the computed hydraulic fracture geometries for newly modeled MIP 3H stages 21 through 28. Figure 2.1 shows the hydraulic fracture geometry for one of the primary induced hydraulic fractures in stage 28 of well MIP 3H. Figure 2.2 shows the cumulative proppant mass versus time (computed vs measured), Figure 2.3 shows the slurry volume injected versus time (computed vs measured), and Figure 2.4 shows the surface pressure versus time (computed vs measured) for stage 28 of well MIP 3H. In general, these figures show a good match between the numerical model and the reported data.

Microseismic data was available for all of the stages modeled during this quarter. Microseismic, well, and hydraulic fracture geometric data were visualized in three dimensions. Figures 2.5 through 2.12 show side views of calculated hydraulic fracture geometries and measured microseismic events and magnitudes for stages 21 through 28, respectively, for well MIP 3H. Figure 2.13 shows an overview of all 8 newly modeled hydraulic fracture geometries, microseismic events, and the entire MIP 3H wellbore. Figure 2.14 shows a top view of all newly modeled hydraulic fracture geometries, microseismic events, and the nearby section of the MIP 3H wellbore. Figure 2.15 shows an orthogonal projection of the newly modeled hydraulic fracture geometries, microseismic events, and the nearby section of the MIP 3H wellbore.

Table 2.1: Computed Fracture Geometries – Stage 21 through Stage 28 – MIP 3H

STAGE	Fracture Half-Length (ft)	Fracture Height (ft)	Average Fracture Width (in)
21	623.8	314.8	0.029267
22	651.9	349.6	0.028956
23	701.8	343.5	0.033113
24	609.3	327	0.02406
25	638.6	331.1	0.030619
26	615	325.5	0.031456
27	585.2	313.4	0.031126
28	629.9	325.5	0.032047

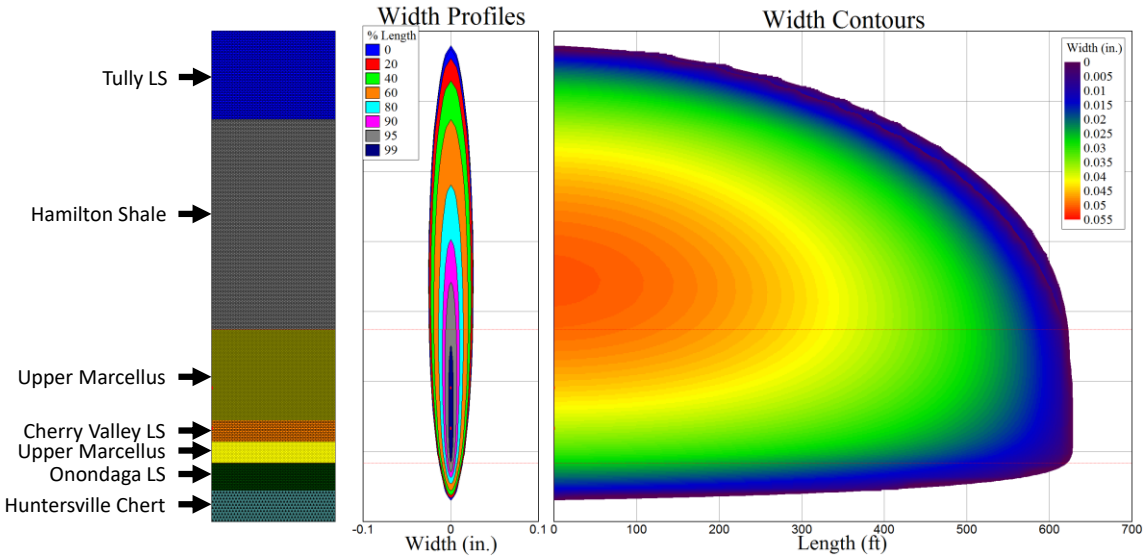

Figure 2.1: Fracture Geometry for Stage 28 - MIP 3H

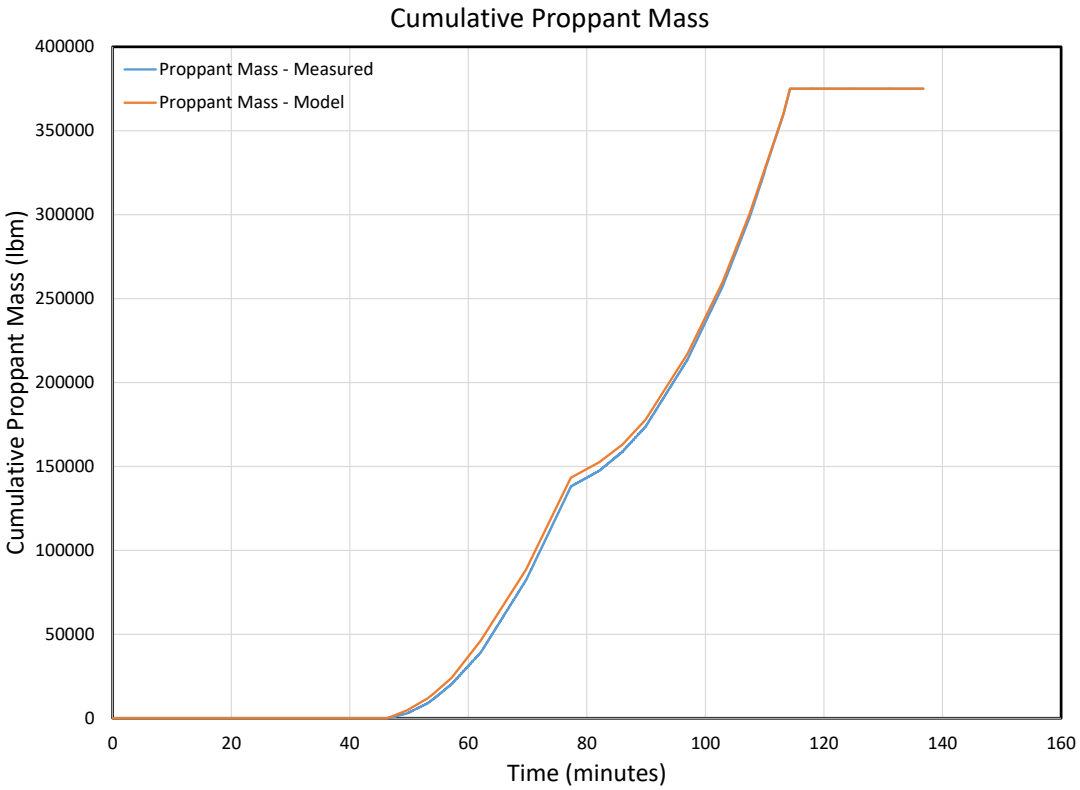

Figure 2.2: Cumulative Proppant Mass for Stage 28 - MIP 3H

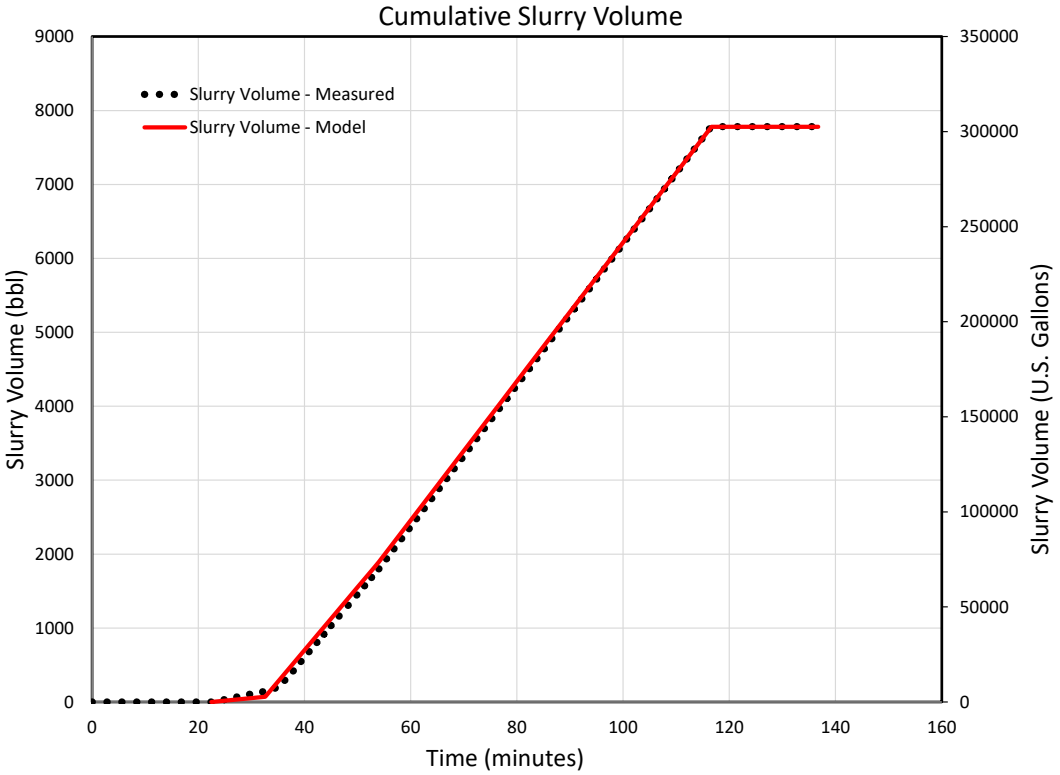

Figure 2.3: Cumulative Slurry Volume for Stage 28 - MIP 3H

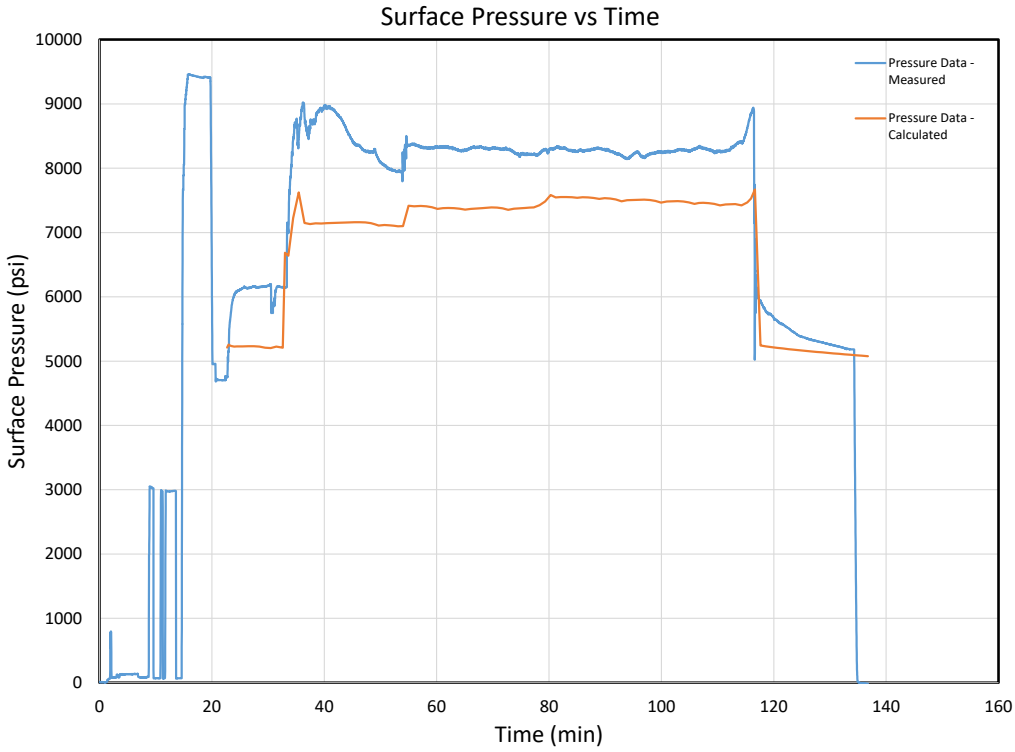

Figure 2.4: Surface Pressure versus Time for Stage 28 - MIP 3H

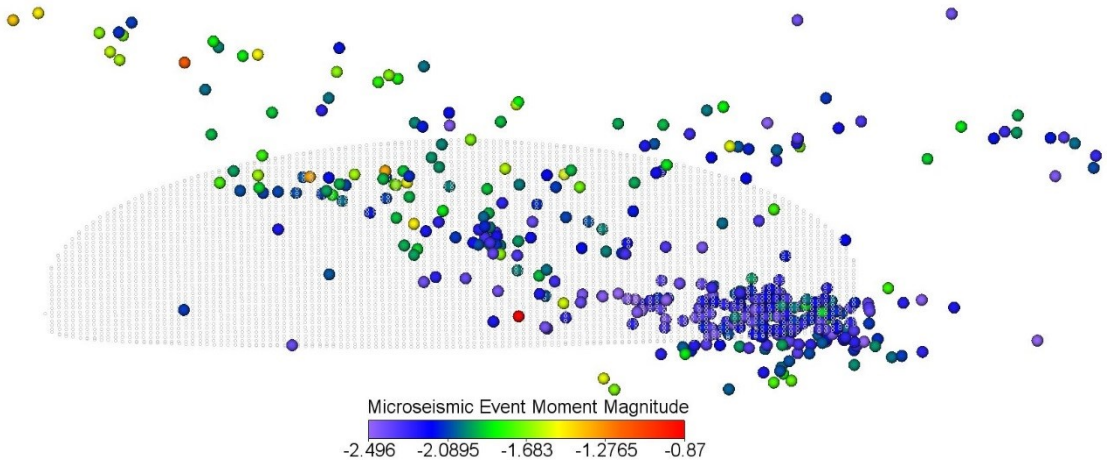

Figure 2.5: Side View of Calculated Hydraulic Fracture and Measured Microseismic Events and Magnitudes for Stage 21 - MIP 3H

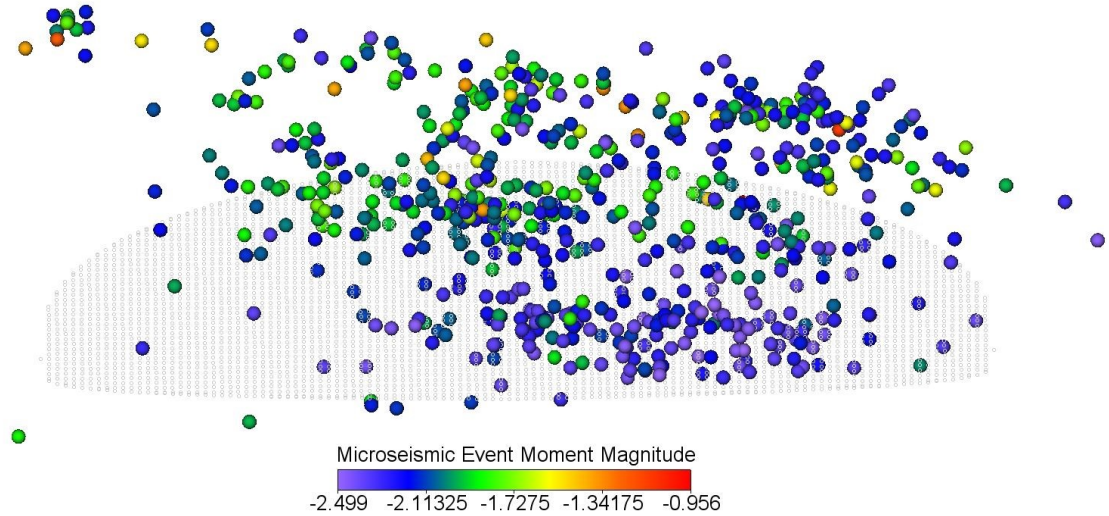

Figure 2.6: Side View of Calculated Hydraulic Fracture and Measured Microseismic Events and Magnitudes for Stage 22 - MIP 3H

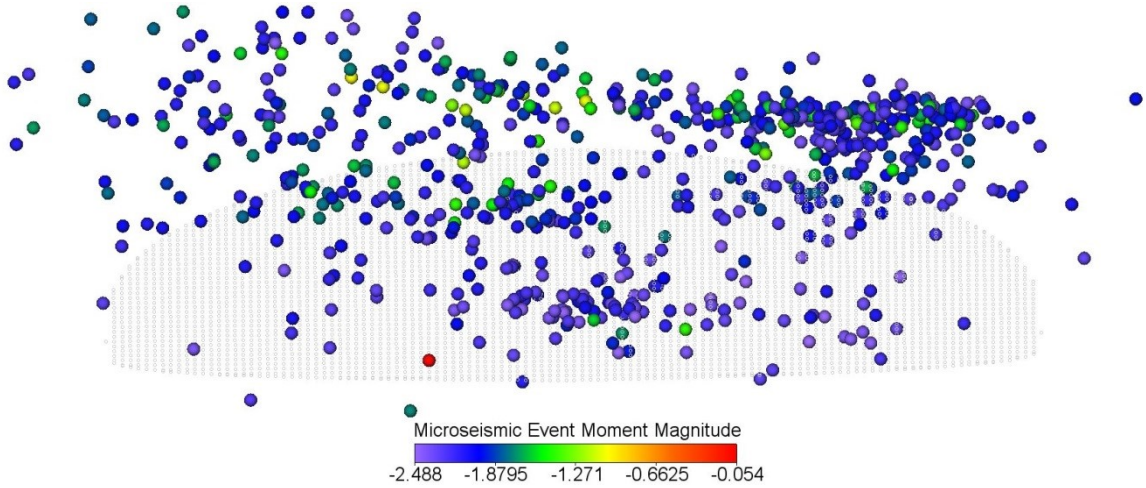

Figure 2.7: Side View of Calculated Hydraulic Fracture and Measured Microseismic Events and Magnitudes for Stage 23 - MIP 3H

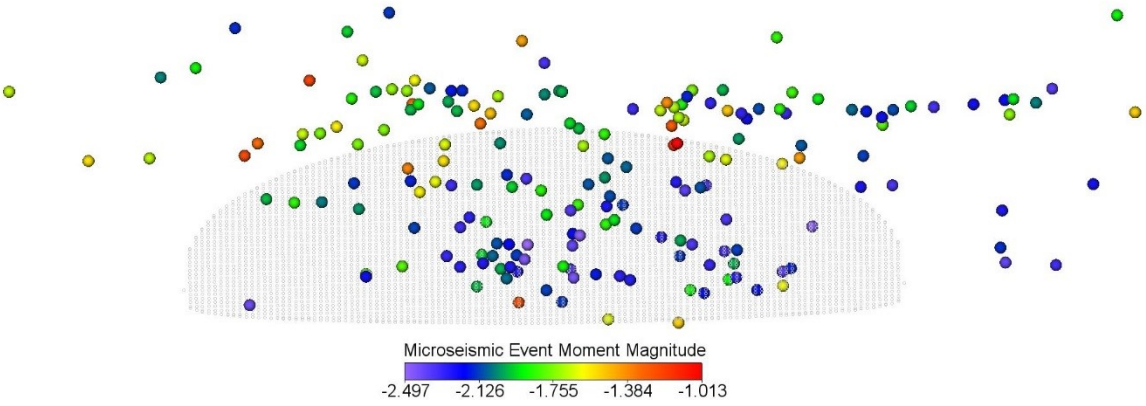

Figure 2.8: Side View of Calculated Hydraulic Fracture and Measured Microseismic Events and Magnitudes for Stage 24 - MIP 3H

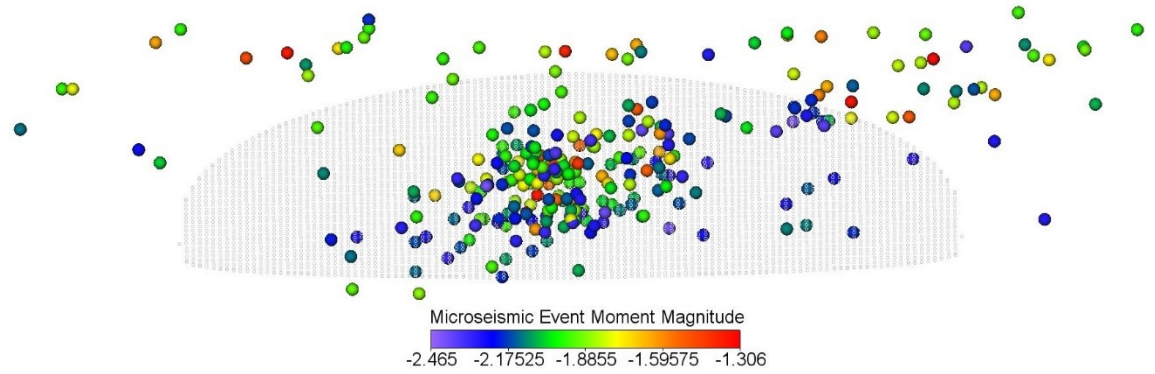

Figure 2.9: Side View of Calculated Hydraulic Fracture and Measured Microseismic Events and Magnitudes for Stage 25 - MIP 3H

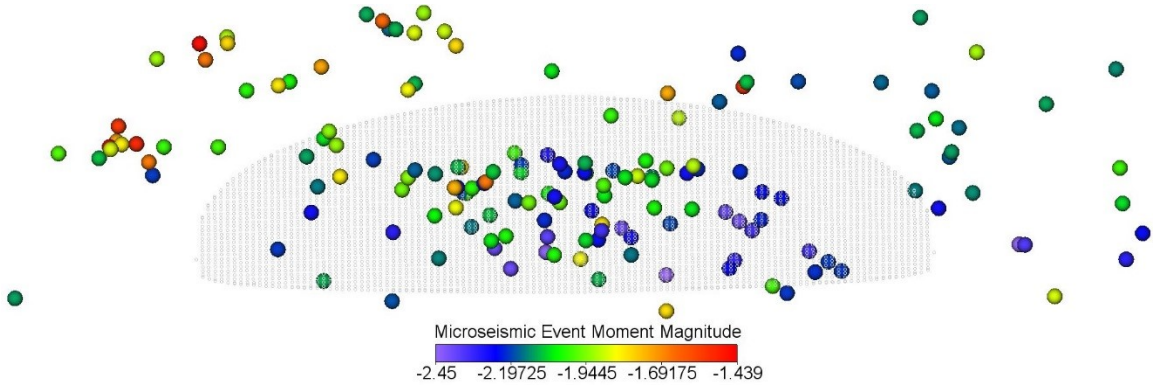

Figure 2.10: Side View of Calculated Hydraulic Fracture and Measured Microseismic Events and Magnitudes for Stage 26 - MIP 3H

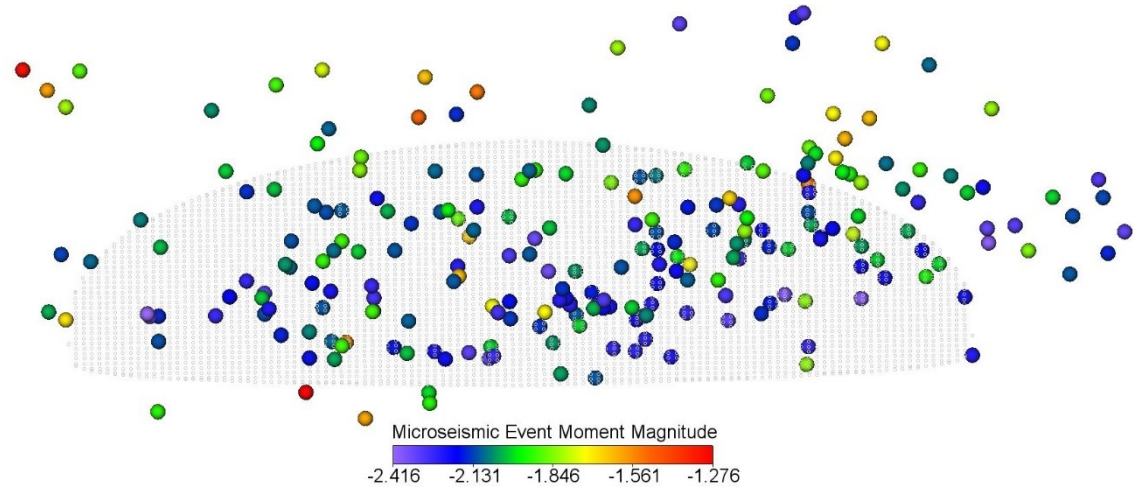

Figure 2.11: Side View of Calculated Hydraulic Fracture and Measured Microseismic Events and Magnitudes for Stage 27 - MIP 3H

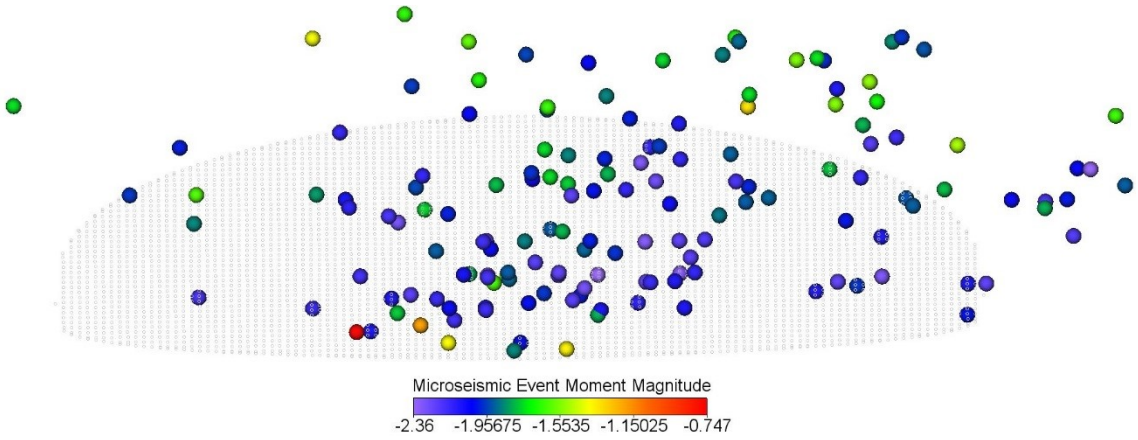

Figure 2.12: Side View of Calculated Hydraulic Fracture and Measured Microseismic Events and Magnitudes for Stage 28 - MIP 3H

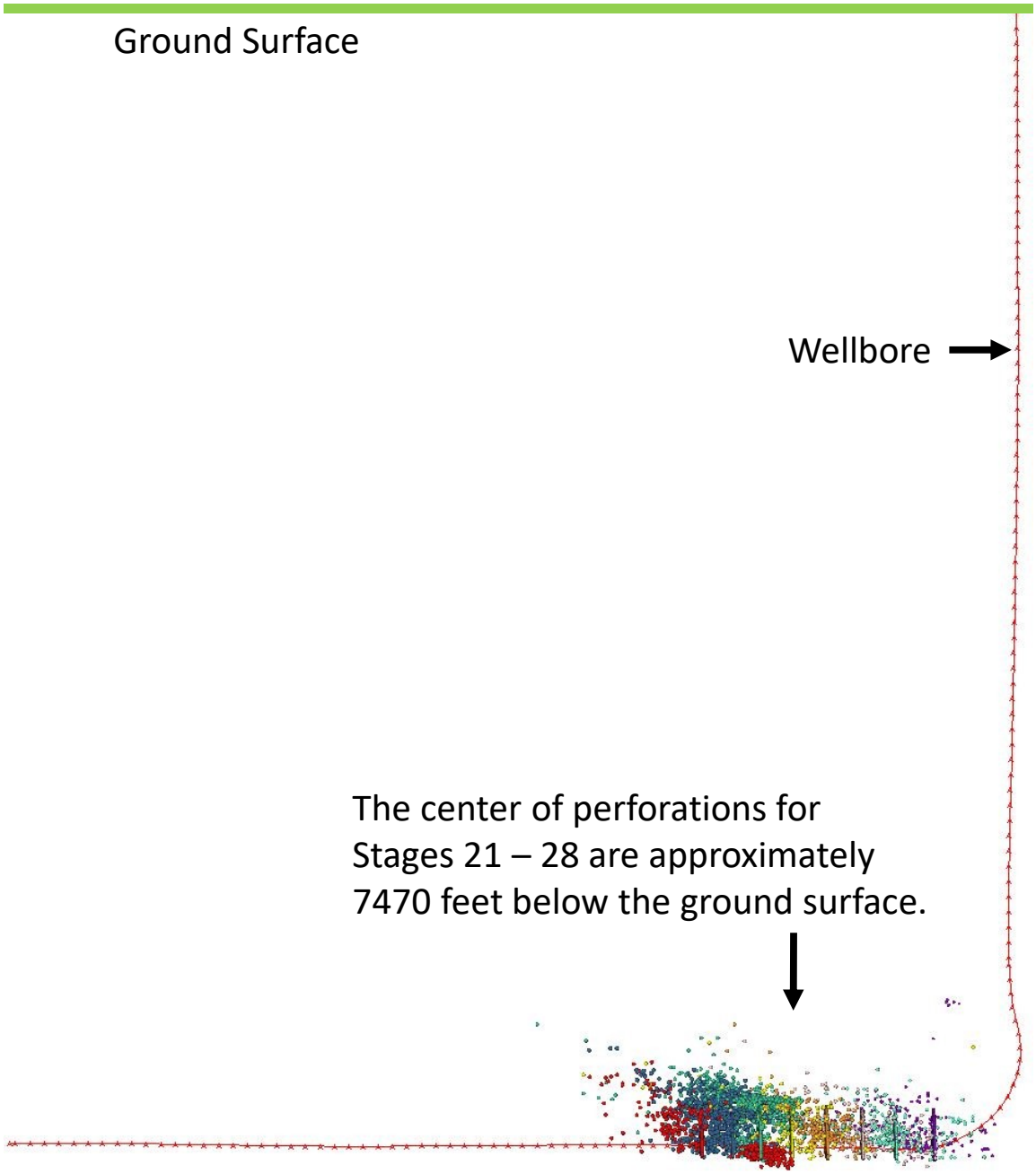

Figure 2.13: Overview of Calculated Hydraulic Fracture Geometries, Measured Microseismic Events, and Entire Wellbore for Stage 21 through Stage 28 - MIP 3H

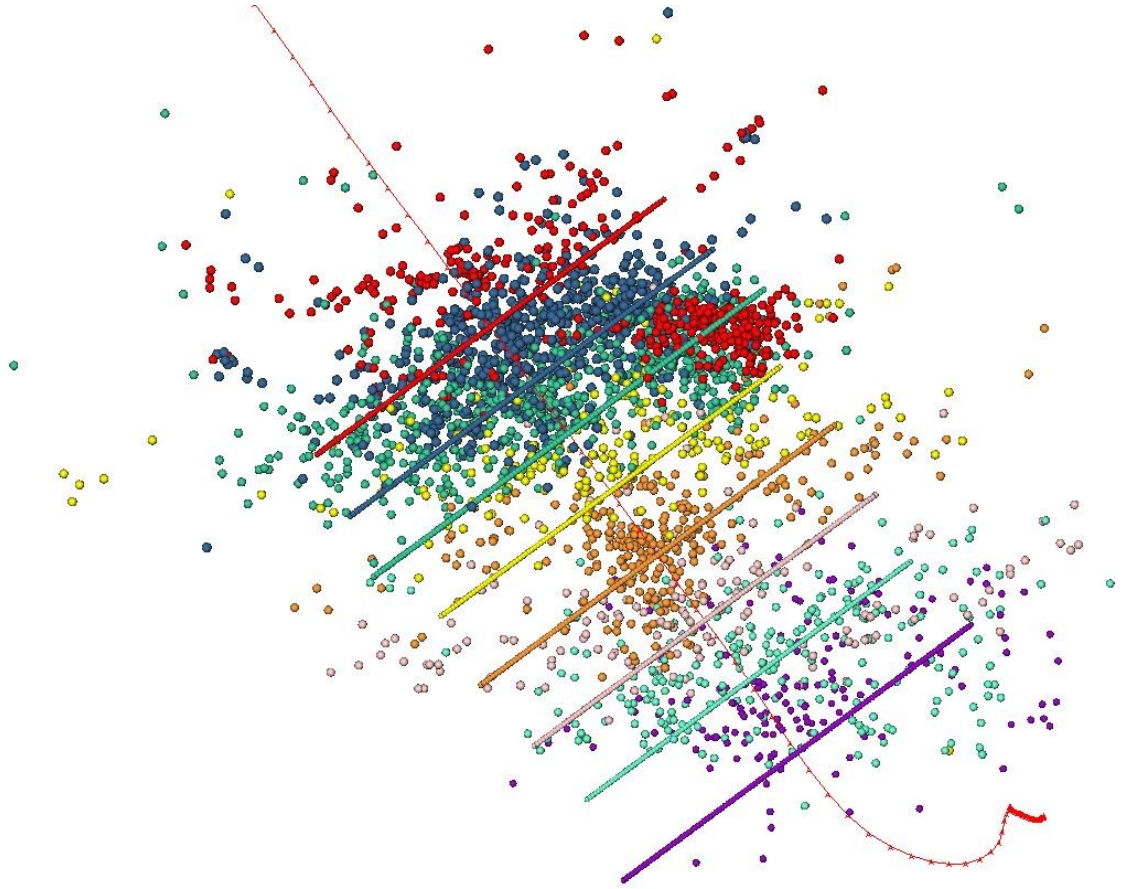

Figure 2.14: Top View of Calculated Hydraulic Fracture Geometries, Measured Microseismic Events, and Nearby Wellbore for Stage 21 through Stage 28 - MIP 3H

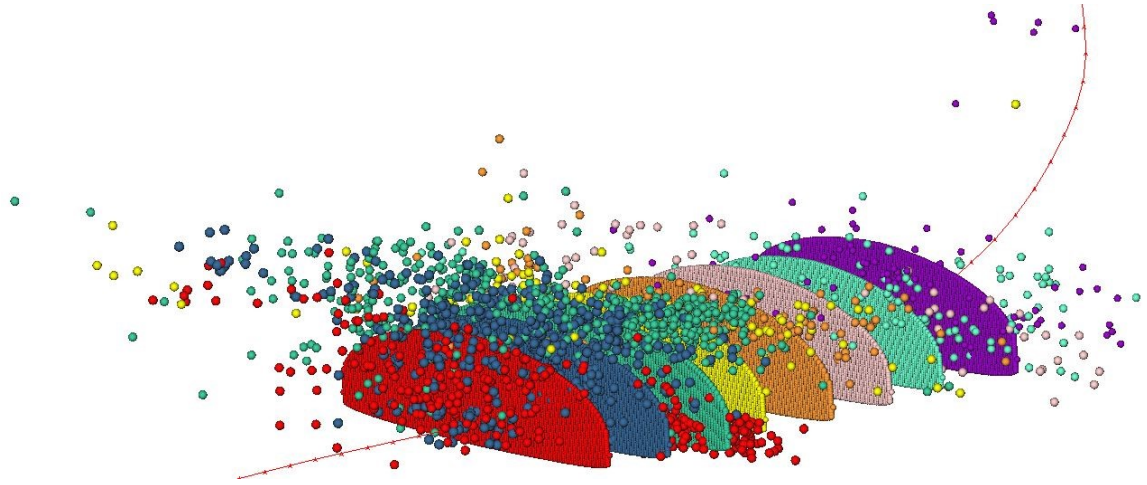

Figure 2.15: Orthogonal View of Calculated Hydraulic Fracture Geometries, Measured Microseismic Events, and Nearby Wellbore for Stage 21 through Stage 28 - MIP 3H

Products

n/a

Plan for Next Quarter

Geophysical

The team will continue to explore the uses of pre-stack AVO inversion in the characterization of unconventional resources. Brian Russell, CGG, will visit the department and present his work on *Adapting conventional seismic reservoir methods for unconventional purposes.*

Geomechanical

With this report, computational modeling for all stages of well MIP 3H has been completed. The modeling study will be continued to investigate stimulation stages at well MIP 5H through the use of available information on the hydraulic fracturing field parameters (fluid volumes, pumping rate, proppant schedule, and geophysical data). The analysis of microseismic data will be continued and a comparison of hydraulic fracture geometries will be made with available microseismic data.

Topic 3 – Deep Subsurface Rock, Fluids, & Gas

Approach

The main focus of the subsurface team led by Sharma this quarter was to analyze core, fluid and gas samples collected from the MSEEL site. Members of Sharma's lab group (Dr. Warrier and Mr. Wilson) and Dr. Hanson from Mouser's lab group continue to coordinate and supervise all sample collections. Samples were also distributed to the research team at OSU and NETL for analysis under different sub-tasks. Several talks and presentations were given at local and regional conferences /universities.

Results & Discussion

Progress on Sidewall Core, Vertical Core & Cutting Aanalysis

The side wall cores are curated at OSU and WVU. Based on the geophysical logs, eight samples were selected from different lithologies, i.e. zones, where maximum biogeochemical variations are expected. Samples were homogenized and distributed among different PI's and are currently being processed for biomarker, isotope analysis, elemental analysis, porosity/pore structure, and noble gas analysis. For the whole core analysis, cores were taken from 1-foot intervals through the 111 feet of whole vertical core. Samples were ground, homogenized, and distributed to different groups at WVU, OSU, and NETL for different analysis.

In **Sharma Lab**, PhD. student Vikas Agrawal analyzed the data generated from the open system pyrolysis (Py-GC-FID) of the kerogen sample extracted from lower Marcellus formation of the MSEEL well. The analysis was done to determine the aliphatic and aromatic carbon chains present in the labile fraction of kerogen as shown in Figure 3.1. The chromatograms generated from the analysis shows the presence of n-alkanes and n-alkenes carbon chains ranging from n-1 to n-12. It also shows the presence of aromatic chains: benzene, toluene, phenol. styrol, xylene,

1,2,4 tetramethyl benzene, naphthalene and 2- methyl naphthalene. The labile aromatic and aliphatic parameters generated will be utilized to construct the structural model by combining

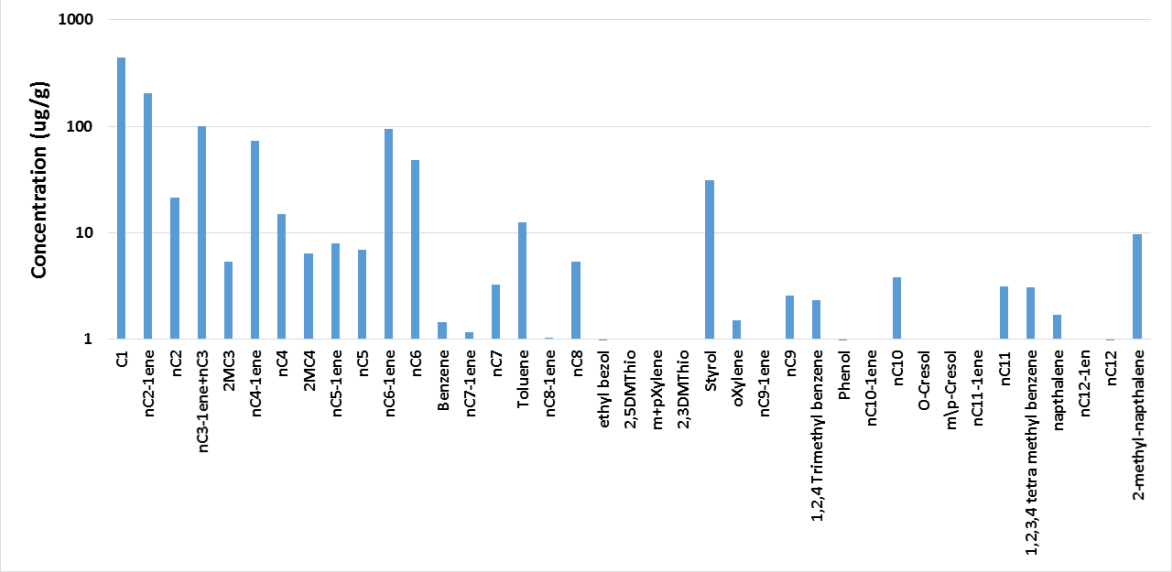

Figure 3.1: Concentration of the aliphatic and aromatic carbon chains present in the labile fraction of kerogen at lower Marcellus formation at the MSEEL site.

The model for kerogen cracking mechanism will also be generated by comparing these structural parameters with those of the lower maturity shales from other parts of Marcellus basin.

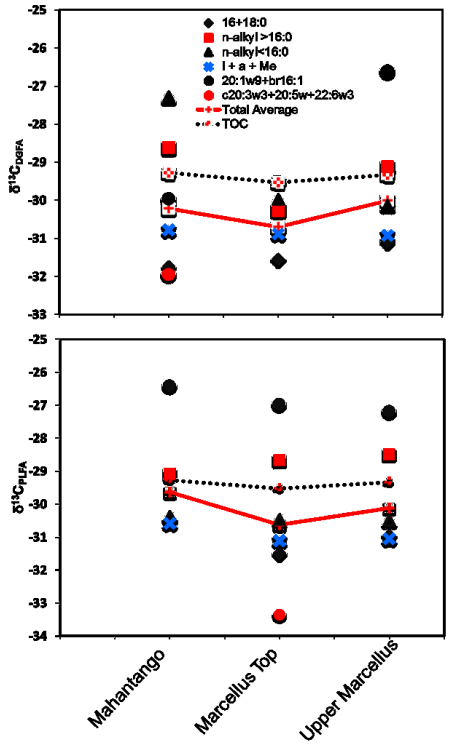

Figure 3.2: Stable carbon isotope ratios for phospholipid fatty acid classes within the sidewall core. The isotope ratios for the compound classes are calculated as mass weighted averages.

Ph.D. Student Rawlings Akondi in **Sharma's Lab** is working on interpreting the compound-specific isotope composition of the diglyceride fatty acids (DGFAs) and phospholipid fatty acids (PLFAs) in the different zones of the sidewall cores. The results indicate that the compound-specific $\delta^{13}C$ analysis of the individual DGFAs range from a maximum of -24.48‰ (n13:0 in the deepest core sample) to a minimum of -33.9‰ (c20:5w3 in shallowest core sample). The compound-specific ^{13}C analysis of the individual PLFAs range from a maximum of -26.48‰ (br16:1) to a minimum of -33.4‰ (c20:3w3 in the transition zone core sample). The isotope values span between 2 and 9‰ for DGFA and 4 and 7‰ for PLFA within single core depths, and individual compounds exhibit up to 6‰ difference in $\delta^{13}C$ values at different core depths for the DGFA. The mass-weighted averages of the $\delta^{13}C$ values were calculated for the total PLFA and DGFA as well as respective compound classes at each core depth (see Fig. 3.1). The mass-weighted averages range from -26.61‰ (in shallowest core) to -31.94‰ (in deepest core) for DGFA and -26.41‰ (in shallowest core) to -33.33‰ (in transition zone core) for PLFA. The transition zone samples exhibit the lowest values for both the $\delta^{13}C_{TOC}$ and the $\delta^{13}C$ of the total PLFA and DGFA. Our results show a clear trend of increasing ^{13}C towards the Mahantango (core top) for individual as well as mass-weighted averages. The $\delta^{13}C$ of the individual lipids show complex patterns of isotopic enrichment and depletions relative to $\delta^{13}C_{TOC}$.

Over the last quarter, **Wilkin's Lab** research group has been finalizing investigations into biofilm formation by the dominant *Halanaerobium* taxa on shale surfaces under representative high-pressure conditions. Results indicate that biomass accumulations on shale surfaces are 4-times greater under high-pressure conditions. Confocal microscopy has been applied to visualize the accumulation of extracellular polymeric substances (EPS, also known as 'slime') on shale material. Scanning electron microscopy has also been applied to the same samples, revealing cell attachment onto shale surfaces and EPS accumulations. Anne Booker presented this work at the American Geophysical Union Fall meeting and work is additionally being written up for submission for publication in February 2018.

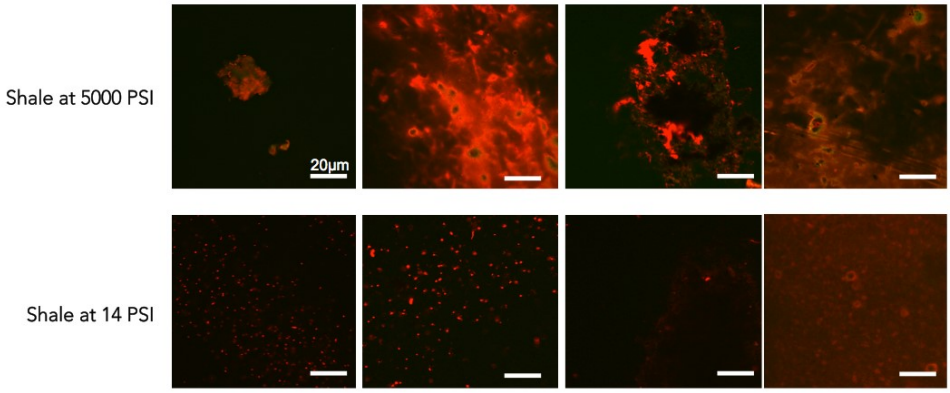

Figure 3.3. Red staining indicates EPS accumulation on shale surfaces.

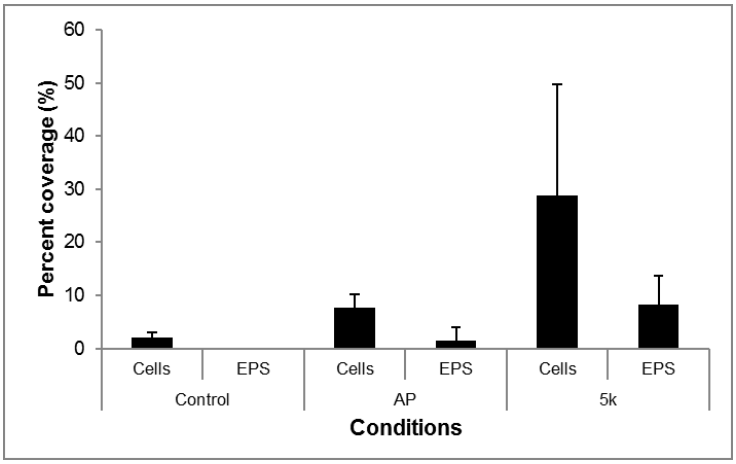

Figure 3.4. Statistical analyses of shale chip– *Halanaerobium* incubations that show increased coverage of shale surfaces by both microbial cells and EPS under 5000-psi growth conditions. AP = atmospheric pressure. Control incubations contained no cells.

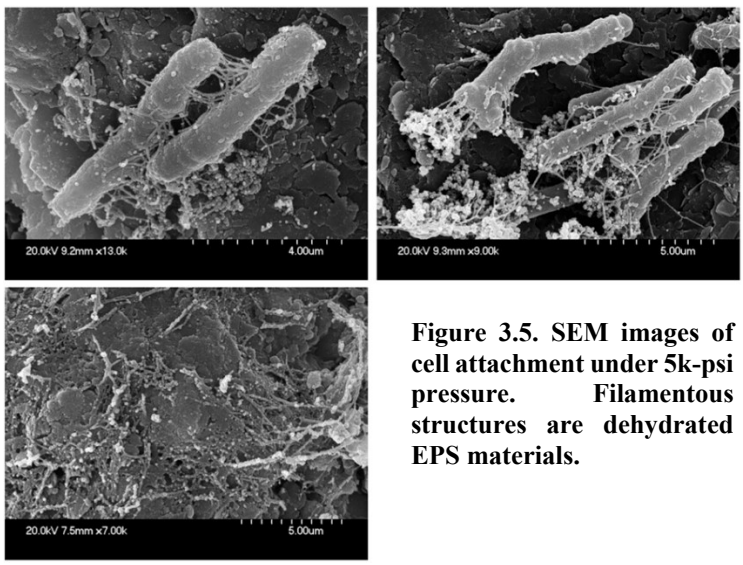

Figure 3.5. SEM images of cell attachment under 5k-psi pressure. Filamentous structures are dehydrated EPS materials.

In **Cole's Lab** a second set of N_2 gas sorption measurements is underway for core samples that are first hand ground to pass through a 60 mesh sieve. This renders the samples to < 250 microns in length scale, which facilitates gas sorption in particle pores. Chips mm in dimension had been attempted first, but these tend to produce poor isotherms. 60-mesh samples were degassed gently (35 degrees C) overnight before acquisition of adsorption and desorption isotherms. No organic separations were conducted prior to analysis, so both mineral and organic matter (OM) pores are interrogated.

Several replicate analyses are measured for each sample, with masses ranging from approximately 0.3-0.6 grams. BET surface area calculations for samples interrogated thus far are greatest for sample ML 10, Lower Marcellus (7543'), the hydraulic fracturing target and the most OM rich among the core suite shared by Cole, Darrah, and Wilkins labs. These BET measurements yield an average specific surface area of around 20 m^2/g. Example isotherm and BET surface area plots are shown in **Figures 3.6a** and **3.6b.**

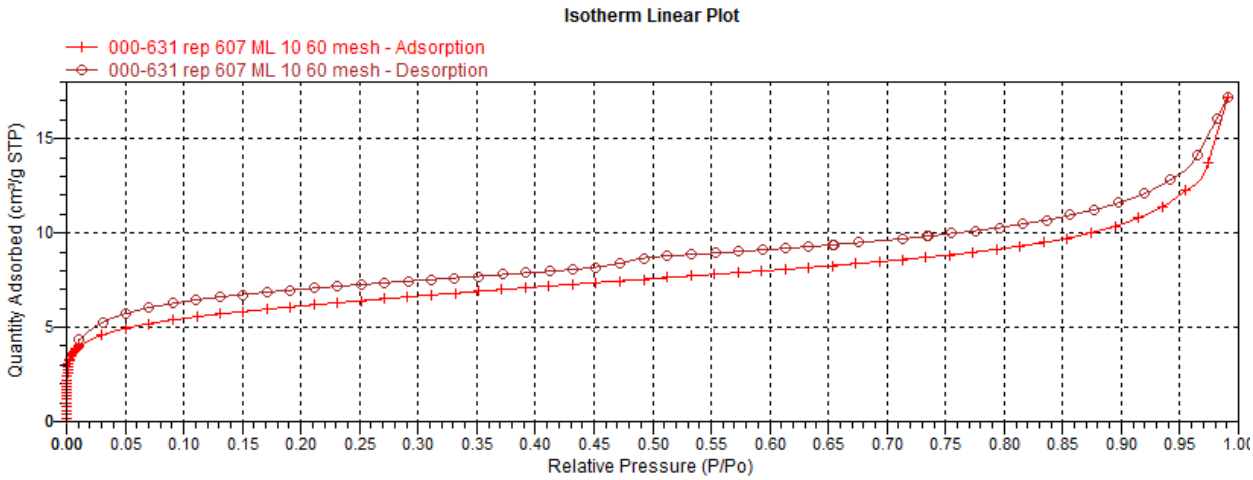

Figure 3.6a. Adsorption and desorption isotherm plot for replicate run 000-631, sample ML 10, Lower Marcellus, depth 7543'

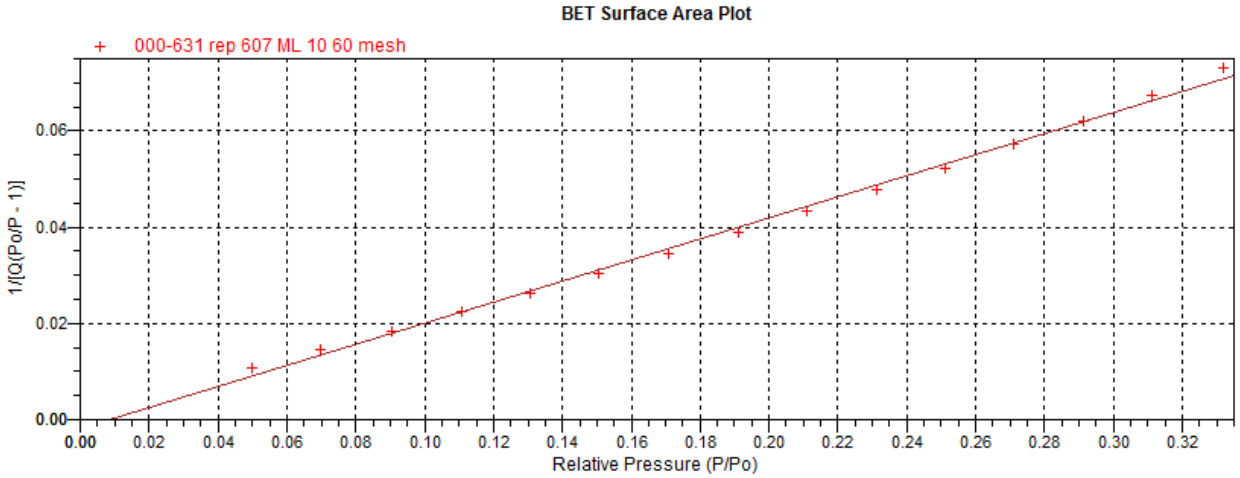

Figure 3.6b. N_2 gas sorption analysis of 60 mesh powder of ML 10 (7543'). BET measurements suggest a surface area of about 20 m^2/g; p/p^o is the relative pressure, referenced to 1 atm.; $[1/Q_{ads}(p/p^o-1)]$ is the normalized moles of adsorbed N_2/gram solid.

Progress on Produced Fluid and Gas Analysis

Produced water samples were collected in 5-gallon carboys in mid-August. The samples were the transported, filtered and processed in Sharma Laboratory at WVU. All water samples were collected in different containers using different methods/ preservatives etc. specified for different kinds of analysis. All PI's at OSU and NETL were provided their detailed sampling instructions. Graduate students John Pilewski and Vikas Agrawal at WVU and Dr. Andrea Hanson from OSU were primarily in charge of sample collection and distribution among different PI's at WVU, OSU, and NETL. The collected fluids are currently being processed for biomass, reactive chemistry, organic acids, and noble gas and stable isotope analysis at different institutes.

Sharma lab continues to analyze O, H, and C isotopic composition of produced fluids collected from 3H and 5H. The carbon isotope composition of the dissolved inorganic carbon in the produced water continues to show the enrichment in ^{13}C with $\delta^{13}C_{DIC} > +17$ ‰ V-PDB and seems to be slowly increasing over time. The isotope analysis of input fluids, sand, cement, reservoir rock and carbonate veins strongly support the microbial utilization of lighter carbon (^{12}C) by methanogenic bacteria in the reservoir. This indicates that introduction of C containing nutrients like guar, methanol, methylamines, etc. could stimulate certain methanogen species in the reservoir to produce biogenic methane in the reservoir. Sharma Lab has also analyzed the carbon isotope signature of produced methane and CO_2 from the produced gas in MIP 3H and 5H. Although the concentration of CO_2 is fairly low in produced gas it does show an increase in $\delta^{13}C$ signature over time, supporting possibility of microbial utilization of $^{12}CO_2$.

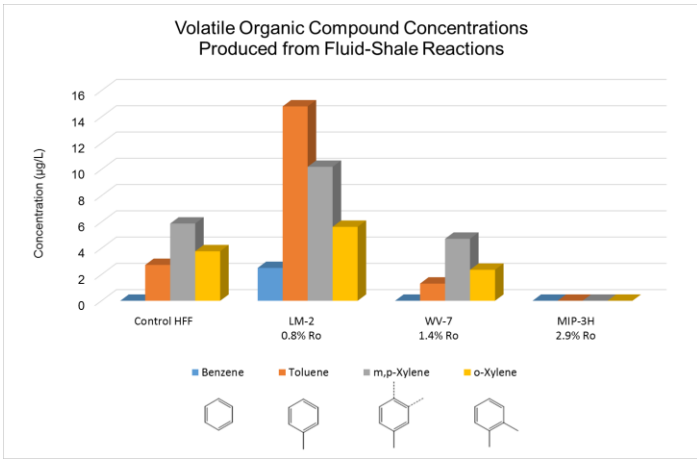

Figure 3.7: Graph showing concentration of key organic compounds after reacting hydraulic fracturing fluid with shales of three different maturities

In **Sharma Lab,** MS student John Pilweski, in collaboration with Hakala lab at NETL, conducted high temperature and pressure fluid-shale reactions using static autoclave reactors in order to emulate and analyze reactions that occur during the shut in phase of hydraulic fracturing operations. Autoclave experiments were carried out for 14 days using a synthetic hydraulic fracturing fluid (HFF) and three samples from the Marcellus Shale. Shale from three different maturity levels were chosen to assess how their different organic matter affects the proliferation of low molecular compounds produced from these reactions. An MSEEL core sample from the MIP-3H well (2.9% Ro) was used to represent the most mature shale. For experimental control the synthetic HFF was subjected to high temperatures and pressure in reactor without any shale. In the control, the team observed production of low molecular weight molecular organic compounds such as toluene and xylene, presumably from the transformation of organic compounds within the synthetic HFF (Figure 3.7). Upon HFF reaction with high maturity shale from MIP-3H, effluent produced showed extremely low concentrations of low molecular weight organic compounds. The opposite trend was observed in effluent produced from reactions with low maturity shale from LM-2 and WV-7, in which produced effluent had the target compounds, benzene, toluene and xylene, at higher concentrations. The preliminary hypothesis is that low

molecular weight organic compounds produced from the transformation of HFF organic additives are being trapped in the organics of high maturity shale. Further investigation and analysis will provide information about where these compounds ultimately end up and how they are transformed during these subsurface reactions.

In the **Mouser's Lab**, Andrea worked with NNE and Sharma's group to collect samples for the team in December and distribute them. Her team also traveled to Colorado State University to analyze hydrophilic organic compounds in MSEEL produced fluids and experimental samples using High Resolution Liquid Chromatography MS (qTOF and QqQ).

Products

Papers Submitted

1. Agrawal V and Sharma S, 2017. Molecular Characterization of Kerogen from Mature Marcellus Shale and its Implications for Determining Hydrocarbon Potential and Thermal Maturity. *Fuel (in review)*
2. Agrawal V and Sharma S, 2017. Use of organic-geochemical proxies to assess organic matter sources, thermal maturity, and paleoredox conditions during deposition of Marcellus Shale. *Frontiers in Earth Sciences (in review)*
3. Akondi R, Sharma S, Trexler R, Mouser PJ, Pfiffner SM, 2017. Understanding Relict Microbial Community Composition in Deep Subsurface Black Shales. *Geomicrobiology (in review)*
4. Luek J, Hari, M, Schmitt-Kopplin P, Mouser PJ, Gonsior M. Temporal Dynamics of Halogenated Organic Compounds in Marcellus Shale Flowback. *Water Research (in review)*
5. Borton, M et. *al.,* 2018In vitro interactions scaled to in situ conditions: microorganisms predict field scale biogeochemistry in hydraulically fractured shale. *Proceedings National Academy of Sciences (in review)*

Presentations

1. Sharma S, Wilson T, Wrighton, K, Borton M & O'Banion. 2017 Can introduction of hydraulic fracturing fluids induce biogenic methanogenesis in the shale reservoirs? Annual American Geophysical Union Conference, Dec 11-15, New Orleans, LA.
2. Booker AE, Borton MA, Daly R, C. Nicora, Welch S, Dusane D, Johnston M, Sharma S et. al., 2017. Potential Repercussions Associated with Halanaerobium Colonization of Hydraulically Fractured Shales. Annual American Geophysical Union Conference, Dec 11-15, New Orleans, LA.
3. Mouser P. *Colorado State University, Civil and Environmental Engineering* and *CSU Water Center*, From the Land Down Under: Microbial Community Dynamics and Metabolic processes influencing organic additives in black shales, 11/2017.

Plan for Next Quarter

Sharma's Lab

PhD student Rawlings will soon start writing the manuscript to be submitted in the journal of Organic Geochemistry. The manuscript will also include a model linking the microbial activities

to the biogeochemical processes (present and past) in these subsurface cores. This study will use the isotopic variation of the microbial species to understand the source of carbon assimilated by the microorganisms. Work will also continue to further analyze results from autoclave experiments.

Cole's Lab

Analysis of fluid samples from the MIP 3H and 5H wells continues. Fluid samples have been analyzed for anions, and prepared for major and trace metal analysis by ICP OES and ICP MS. Analysis of precipitates and colloidal material, pipetted from the bottom of containers of flowback and filtered (both fresh and year-old brine samples from the 3H well) is ongoing. More SEM observations of precipitates forming in flowback fluids have been generated.

Mouser's Lab

No Input

Wilkins's Lab

Work will continue to finish a February 2018 publication on investigations into biofilm formation by the dominant *Halanaerobium* taxa on shale surface.

Darrah's Lab

Worked continues on time-series analysis of fluid samples collected monthly from the MIP 3H and 5H wells. The major focus in this and the following quarter has transitioned from sample analyses to data interpretation and publication in the last quarter.

Topic 4 – Environmental Monitoring – Surface Water & Sludge

Approach

The Marcellus Shale Energy and Environment Laboratory (MSEEL) is the first comprehensive field study coupling same site environmental baseline, completion and production monitoring with environmental outcomes. Almost two years into the post completion part of the program, the water and solid waste component of MSEEL has continued to systematically sample flowback and produced water volumes. During year one of the study, hydraulic fracturing fluid, flowback, produced water, drilling muds and drill cuttings were characterized by their inorganic, organic and radio chemistries. In addition, surface water in the nearby Monongahela River was monitored upstream and downstream of the MSEEL drill pad. Toxicity testing per EPA method 1311 (TCLP) was conducted on drill cuttings in both the vertical and horizontal (Marcellus) sections to evaluate their toxicity potential.

Previous findings

The MSEEL wells used green completion strategy including a synthetic based drilling fluid (Bio-Base 365). All drill cutting samples fell below TCLP thresholds for organic and inorganic components indicating that they are non-hazardous per the Resource Conservation and Recovery Act. Maximum specific isotopic activity in drill cuttings was recorded for 40 K which was 28.32 pCi/g. Gross alpha accounted for the highest reading at 60 pCi/g. The maximum combined radium isotope values was 10.85 pCi/g. These radioactivity levels are within the background range for the region.

The composition of the hydraulic fracturing (HF) fluids in both wells was similar to the makeup water which was drawn from the Monongahela River. Its chemistry was typical of Monongahela River water. This is true of inorganics, organics and radio chemicals. Organic surrogate recoveries were in the range of 90 to 104% indicating good quality control at the analytical laboratory. There was no evidence that Monongahela River quality was influenced by well development, completion or production at the MSEEL site.

Produced water is severely contaminated indicating care in handling. Concentrations of all parameters increased through the flowback/produced water cycle. 226+228 Ra reached 20,000 pCi/L at post completion day 251 indicating an important trend that will be carefully assessed in ongoing monitoring.

Methods

Sampling schedule

Table 4.1 summarizes the produced water sampling schedule for the quarter. Produced water samples were taken at the upstream end of each well's separator.

Table 4.2: Sampling schedule for the quarter.

	Freshwater		Aqueous/Solids: drilling/completion/production								
	Mon River	Ground water	HF fluid makeup	HF fluids	flowback/ produced	drilling fluids	drilling cuttings/ muds	total aqueous	total solids	Sampling Dates	Sampling Notes
Sampling Stations											
Flowback @ 93 weeks - 3H					1			1		9/20/2017	one sample 3H
Flowback @ 93 weeks - 5H					0			0		9/20/2017	5H offline
Flowback @ 300 weeks 4H					0			0		9/20/2017	4H offline
Flowback @ 300 weeks 6H					0			0		9/20/2017	6H offline
Flowback @ 99 weeks - 3H					1			1		11/3/2017	one sample 3H
Flowback @ 99 weeks - 5H					0			0		11/3/2017	5H offline
Flowback @ 306 weeks 4H					0			0		11/3/2017	4H offline
Flowback @ 306 weeks 6H					0			0		11/3/2017	6H offline

Subtask 2.2.1b for Year 2 "produced water precipitate and perform toxicity and radiochemistry analyses" has been initiated. Preliminary results will be included with the next quarterly report.

Analytical parameters

Analytical parameters analyzed for samples flowback produced water (FPW) collected are listed in Table 4.2.

Table 4.3: Aqueous analytical parameters for FPW analyzed.

Aqueous chemistry parameters - HF fluids and FPW***						
Inorganics					Organics	Radionuclides
	Anions		Cations*			
pH	Br		~~Ag~~	Mg	Benzene	α
TDS	Cl		Al	Mn	Toluene	β
TSS	SO_4		As	Na	Ethylbenzene	^{40}K
Conductance	sulfides		Ba	Ni	Total xylene	^{226}Ra
Alkalinity	nitrate		Ca	Pb	m,p-xylene	^{228}Ra
Bicarbonate	nitrite		Cr	Se	o-xylene	
Carbonate			Fe	Sr	MBAS	
TP			K and Li	Zn	O&G	

Results & Discussion

Produced water volume trends in wells MIP 3,5H and MIP 4,6H

NNE's water production logs were used to estimate produced water volumes. While water production rates were similar in the first two months post completion, cumulative water production rates soon diverged yielding very different curves for each well (figure 1). It is noted that the older wells (4H, 6H) were shut in between 12 Dec 15 and 17 Oct 16, an interval of 315 days.

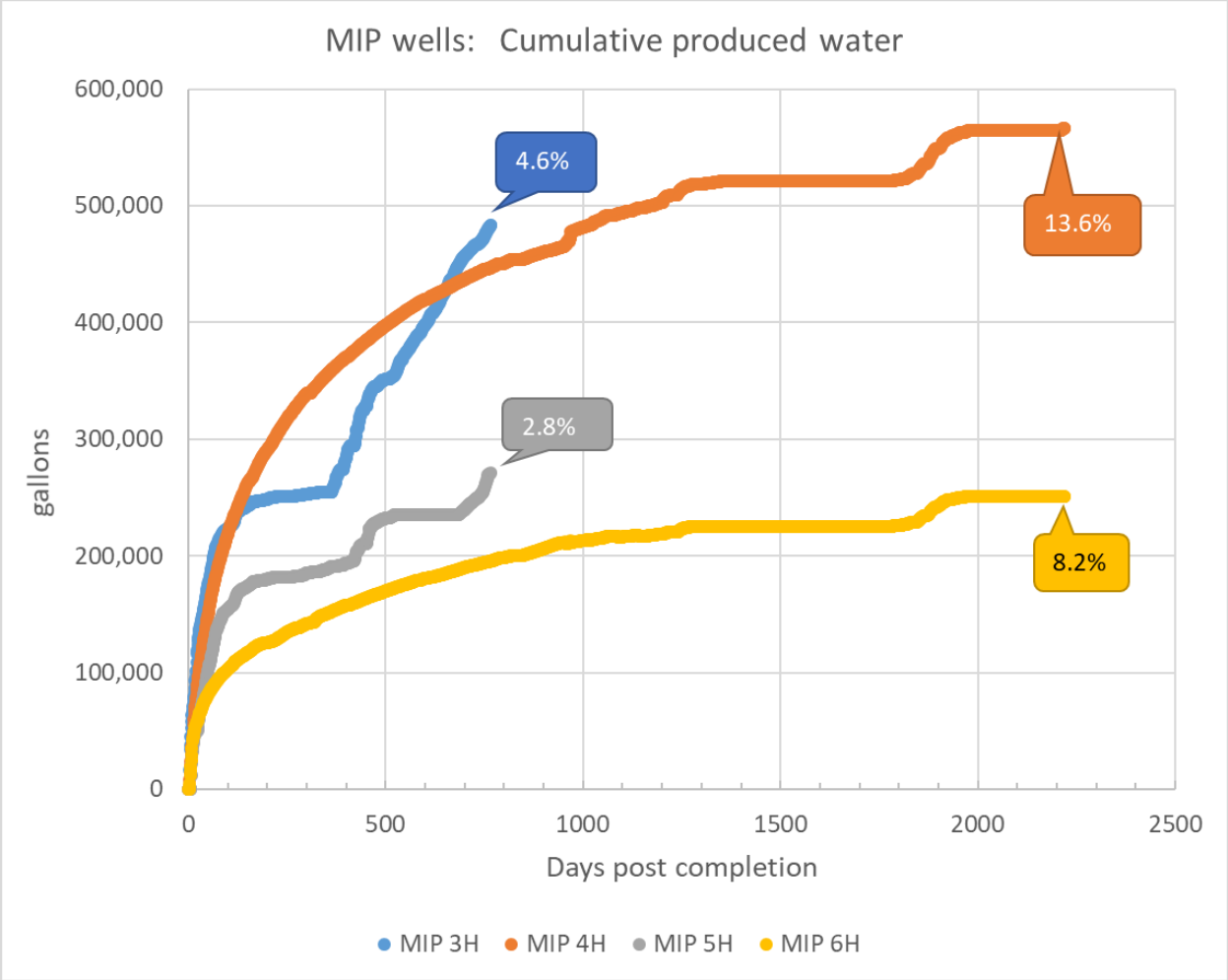

Figure 4.1: Cumulative water production at the four MSEEL wells.

The proportion of hydrofrac fluid returned as produced water, even after 2219 days (6 years) was only 13% at MIP 4H and 8.2% at MIP 6H (Table 4.3). The reason for the variation among wells both respect to cumulative and proportional produced water returns remains an unanswered question.

Table 4.3: Produced water volumes relative to injected HF fluid for each MSEEL well

	days post completion	cumulative produced water gal	cumulative produced water % injected	HF injected gal	HF injected m^3
MIP 3H	766	482,977	4.6%	10,404,198	39,380
MIP 5H	767	271,985	2.8%	9,687,888	36,669
MIP 4H	2219	540,552	13.0%	4,160,982	15,749
MIP 6H	2219	250,905	8.2%	3,042,396	11,515

Trends in produced water chemistry

Major ions

While makeup water was characterized by low TDS (total dissolved solids) and a dominance of calcium and sulfate ions, produced water from initial flowback is essentially a sodium/calcium chloride water (Figure 4.2). Other than slight increases in the proportion of barium and strontium, the ionic composition of produced changed very little through 580 days post completion.

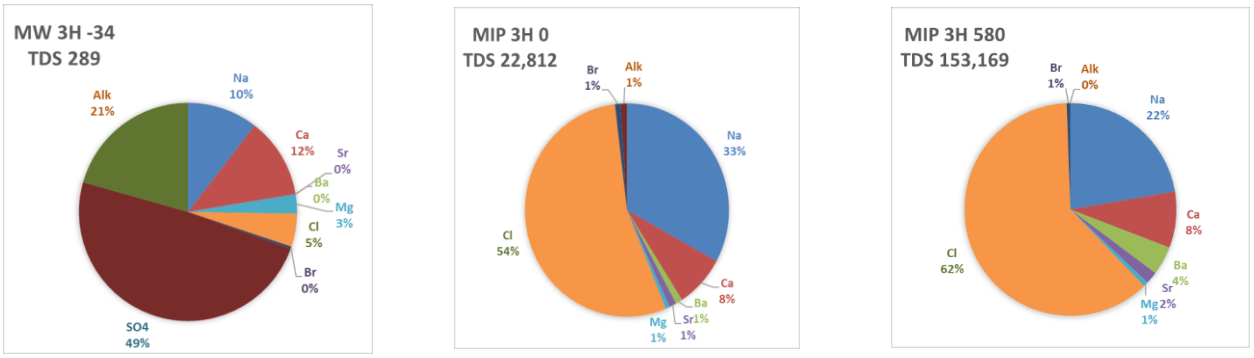

Figure 4.2: Changes in major ion concentrations in produced water from well MIP 3H. From left to right the charts represent makeup water from the Monongahela River, produced water on the first day of flowback and produced water on the 580th day post completion.

In fact, after 1,963 days, ionic composition remained nearly identical to the initial produced water (Figure 4.3) while TDS declined.

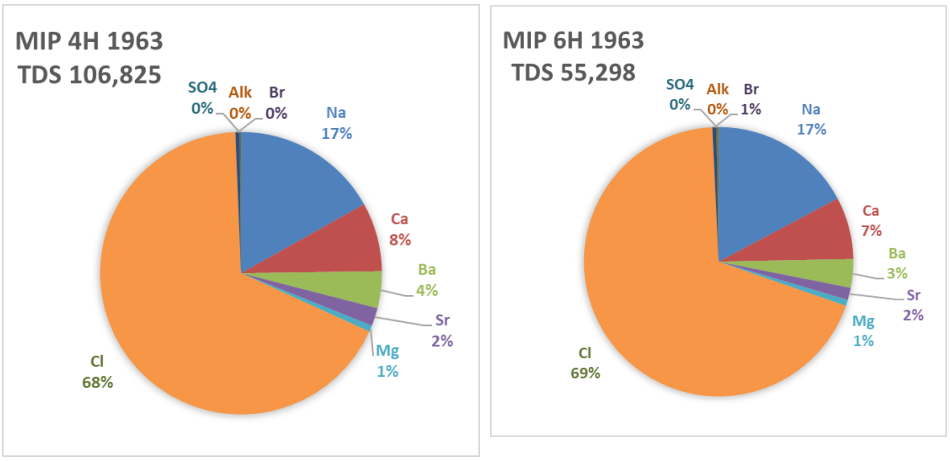

Figure 4.3: Major ion composition of wells MIP 4H and 6H 1935 days after completion.

Water Volume

The volume of produced water decreased rapidly from nearly 500 bbl/day to less than 1 bbl/day after one year. It then increased. Over this cycle produced water averaged about 16 bbl/day. After six years, cumulative flowback and produced water represented only 8.2 and 13.6% of injected fluids at wells 6H and 4H respectively. After 767 days only 2.8 and 4.6% reported to the wellhead at the 5H and 3H wells respectively (Figure 4.4).

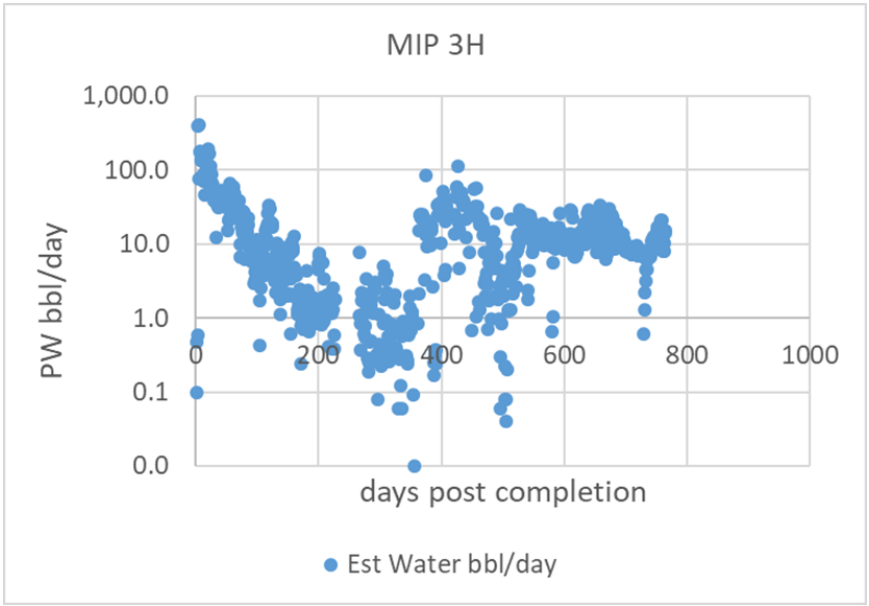

Figure 4.4: Produced water barrels (bbl) per day post completion.

While TDS increased rapidly over the initial 90 days post completion values had been consistently between 100,000 and 150,000 mg/L through day 694 and have since continued on an upward trend, increasing to around 190,000 mg/L for 3H (Figure 4.5). The older 4H and 6H wells offer insight into the longer term TDS trend. Those wells only came back on line during

this quarter after a shut in period of 315 days and those results vary but they are much lower than the current values for wells MIP 3H and 5H.

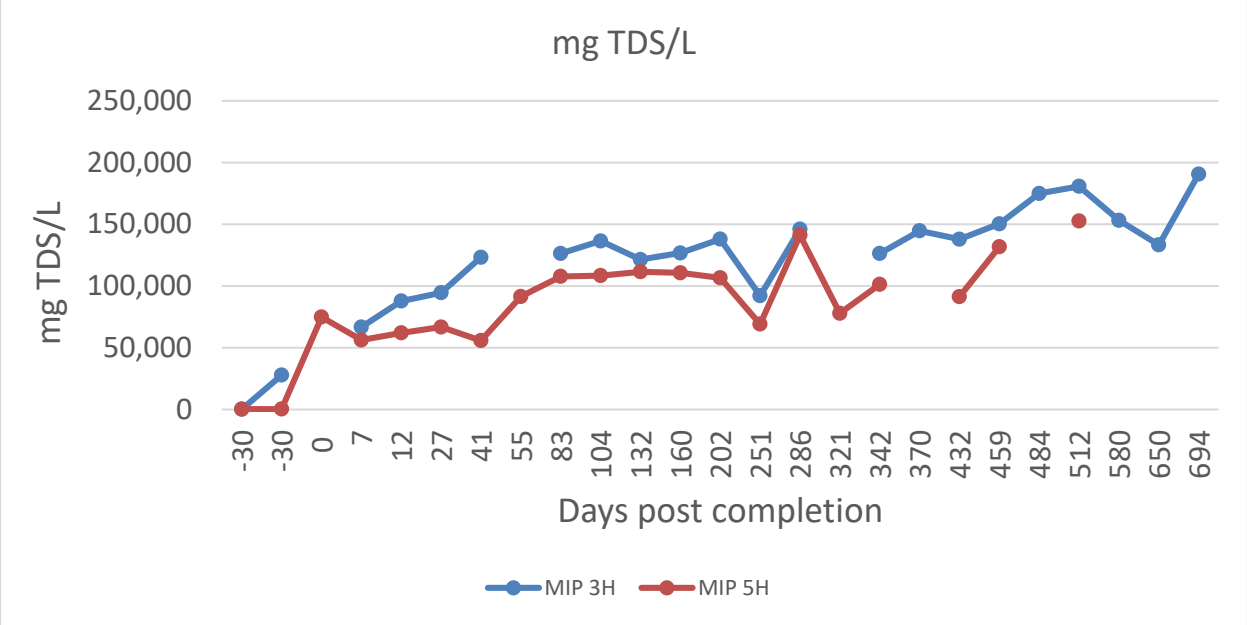

Figure 4.5: Changes in produced water TDS sdc (sum of dissolved constituents) through the first 694 days post completion (3,5H).

Water soluble organics

The water soluble aromatic compounds in produced water: benzene, toluene, ethylbenzene and xylene were never high. With two exceptions at post completion day 321 and 694, benzene has remained below 30 µg/L (figure 6) (we are awaiting confirmation from the analytical lab for this reported value of 41 µg/L for day 694). Apart from the spikes, this seems to be a characteristic of dry gas geologic units. After five years, benzene has declined below the drinking water standard of 5 µg/L.

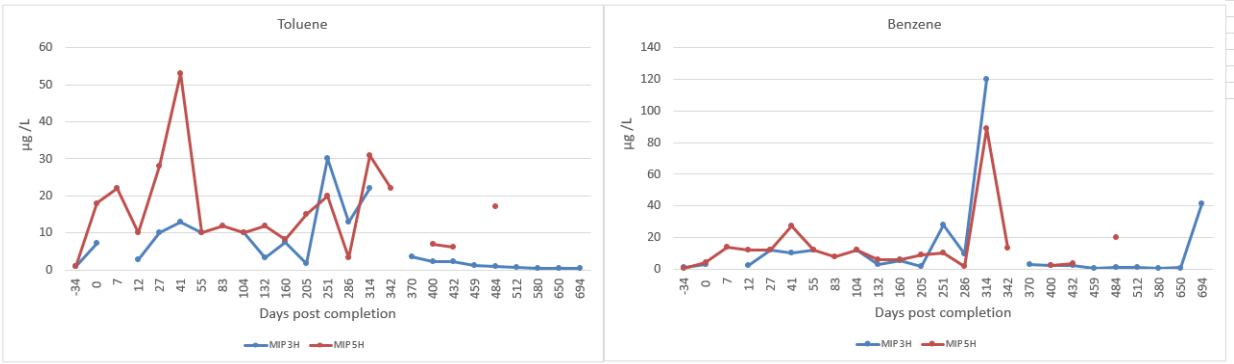

Figure 4.6: Changes in benzene and toluene concentrations. The figure shows data from well both 3H and 5H.

Radium isotopes

Radioactivity in produced water

Radium concentrations generally increased over the 694 days post completion at wells MIP 3H and 5H. Maximum levels of the radium isotopes reached about 20,000 pCi/L at the unchoked 3H well and about half that amount at 5H (Figure 4.7).

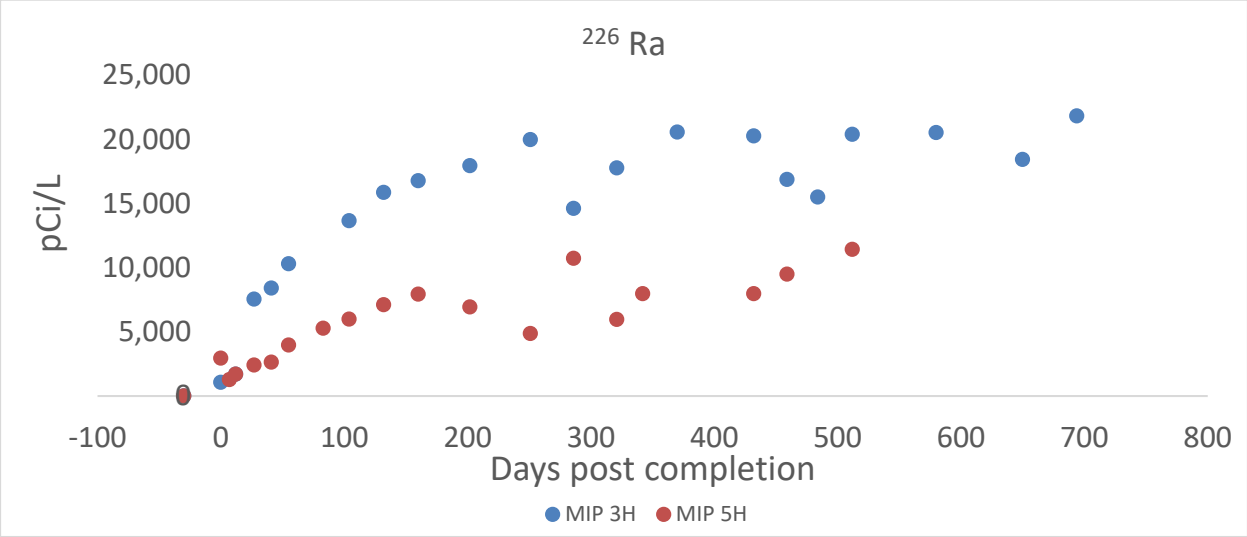

Figure 4.7: The radium isotopes are plotted against days post well completion. Well 5H was choked periodically. It produced less water and lower concentrations of radium.

At the older wells MIP 4H and 6H, all isotope concentrations declined to low levels, often below the MDC (minimum detectable concentration) (table 4). This, like the apparent decline in TDS at the older wells is an interesting result and, if sustained by future sampling, would suggest exhaustion of contaminant reserves within the fracture field.

Table 4.4: Radiochemistry of the older wells 4H and 6H at 1828 (5 years) days post completion.

		16-Nov-16 MIP 4H days post completion: 1828			16-Nov-16 MIP 6H days post completion: 1828		
		act[1]	unc[2]	mdc[3]	act[1]	unc[2]	mdc[3]
α	pCi/L	228.0	53.6	27.2	57.7	10.9	1.6
β	pCi/L	48.7	20.1	29.2	7.4	1.6	0.8
^{226}Ra	pCi/L	353.3	260.6	309.2	199.3	333.5	390.3
^{228}Ra	pCi/L	31.1	31.9	48.6	0.0	20.9	54.6
^{40}K	pCi/L	49.7	95.5	102.7	0.0	21.9	151.4

[1] activity

[2] +/- uncertainty

[3] minimum detectable concentration

The radiochemical concentrations were determined by Pace Analytical in Greensburg PA, a state certified analytical lab. Figure 4.8 shows the relationship between gross alpha and ^{226}Ra. The relationship between alpha and ^{226}Ra is clear but the correlation coefficients show much more variance in the alpha readings. So, individual values can diverge to a far greater extent than the modelled values. Earlier studies e.g. Ziemkiewicz and He 2015 often relied on samples taken from several wells over short time spans so the apparent differences between alpha and, individual isotope concentrations may well be analytical artifact. The MDCs and uncertainty levels reported by the lab indicated that both the alpha and radium levels were within ranges that would be considered reliable. This may illustrate the limitations of survey level parameters such as gross alpha.

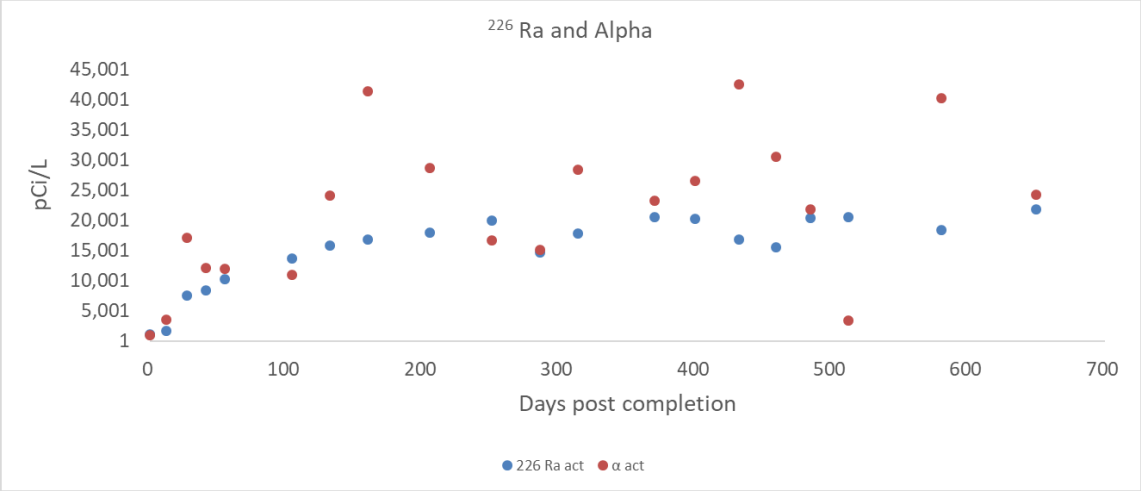

Figure 4.8: The relationship between gross alpha and ^{226}Ra as a function of time post completion.

Products

Presented "Marcellus Shale Energy and Environmental Laboratory: Water and Waste" for Independent Oil and Gas Association, Charleston WV.

Plan for Next Quarter

Next quarter, the team will continue to sample and analyze flowback/produced water (FPW) from MIP 3H on a quarterly basis, and other wells at 4H, 5H and 6H if they go back online. The team will also collect for subtask 2.2.1b "produced water precipitate and perform toxicity and radiochemistry analyses" and begin development of chemical hygiene plan and set up for experiments of subtask 2.2.1c "chemical and biological factors influencing precipitate formation."

References

Ziemkiewicz, P.F. and He, Y.T. 2015. Evolution of water chemistry during Marcellus shale gas development: A case study in West Virginia. Chemosphere 134:224-231.

Topic 5 – Environmental Monitoring: Air & Vehicular

Approach

Air

The techniques of trace element analysis, satellite Aerosol Optical Depth, in-situ measurements, distance and depth of well are being used to assign dose in communities near hydraulic fracturing operations. Each method has its strength and weaknesses but they have not previously been compared. Being able to perform simultaneous assessments of all of these techniques has been possible for an experimental well drilled in West Virginia, using standard operating techniques by the drillers who were cooperating with the monitoring program.

Results indicate that for the river valley topography of the region it was possible to assess some exposure from the well pad to the surrounding community at a distance of at least 7 km. This was done using trace quantities of airborne magnesium analyzed from high volume filter samples. Simultaneously, PM2.5 concentration data was collected using direct-reading photometric analyzers. These dust concentration values were shown to compare favorably to MODIS satellite data for analysis of aerosol optical depth (AOD) for a number of nearby locations. The satellite AOD measurements were then compared to previously proposed, indirect measures of community exposure derived from distance to the well and natural gas production values for surrounding sites.

Vehicular

This quarterly report includes the results of a fourth MSEEL site audit focused on in-use methane emissions. The data from all four audits have been analyzed and compared to literature data in a draft article submitted to Geophysical Research Letters. The following update includes summary data from the draft publication.

Direct quantification methods were used with a custom full flow sampling system with an uncertainty of ±10%. Other studies have included indirect methods such as dispersion modelling of plumes or using tracer release methods. Results follow trends suggested by sampling multiple sites: a majority of emissions are attributed to a smaller number of emitters and methane emissions are highly variable. The total methane emissions from our site varied between 39.7 to 4103.8 g/hr with a mean of 1647.7 g/hr. The largest source of emissions from all audits was the produced water storage tank (PWST) – 3.7 kg/hr. Site-wide methane emissions tended to increase as throughput increased. From this data, it is shown that repeated measurements at sites may yield significantly different results over time. If the average site emissions of 1647.7 g/hr are representative – using a single audit could have under estimated emissions by a factor of 104 or overestimated site emission by factor of 2.5. Thus, even with labor intensive and accurate site audits, methane emissions remain highly variable and a single snapshot in time may not accurately reflect annual emissions.

Results & Discussion

Air

Trace magnesium concentration does appear to be a method for assessing environmental exposure for the time and location used in this study. The distances at which measureable amounts of magnesium could be found exceed, substantially, previous estimates. This could

provide a rationale for the findings of health effects outside the previous limits of detectable air emissions. The valley along which sampling occurred, however, may act to funnel the air contaminants and retard dispersion. Traffic from the well pad could not be ruled out from the current work as another source of wide spread air contaminant emissions. Further work is planned to use the tools assessed here to provide more information on that question.

Vehicular

Table 5.1 presents the emissions by source for the fourth audit. Only a single leak was detected and quantified during this audit that was not related to other source categories. The largest contributor was again the PWST and small unloading events that were occurring throughout the audit. A new emissions source was identified – a new methanol injection system (MIS) was installed onsite and its operation used NG as the working fluid. Its emissions represented 30.6% of the total emissions.

Table 5.1: Audit 4 Results by Source – EGPU, enclosed gas production unit; UHW, unconventional well head.

Source	CH_4 Emissions Rate					Contribution
	SCFM	g/sec	g/hr	kg/day	kg/yr	%
Leaks	0.005	0.002	6.04	0.14	52.91	0.3
MIS	0.445	0.150	539.96	12.96	4730.05	30.6
PWST	0.851	0.287	1032.31	24.78	9043.04	58.4
EGPUs	0.155	0.052	188.20	4.52	1648.63	10.6
UHWs	0.001	0.000	0.82	0.02	7.16	0.0
Total	1.457	0.491	1767.327	42.416	15,481.78	100.0

Figure 5.1 presents the cumulative site emissions. Audits 1 and 2 do not include stack emissions but if the emissions were similar to those during Audits 3 and 4, their impact would be less than 1%.

Figure 5.1 includes a break down by the major categories of UWHs, PWST, EGPUs, and other. Other includes emissions from stacks, leaks, and other sources. The total for Audit 3 includes stack emissions which were measured and only one EGPU was in operation. Audit 4 total methane emissions includes twice the measured value since both EGPUs were in operation. Error bars represent the ±10% measurement error. Also included in Figure 5.1 is a line for the arithmetic mean of the emissions from the four audits and the arithmetic mean and geometric mean of well site emissions rates presented by Rella et al. (2015). The figure shows that cumulative emissions varied significantly throughout the year ranging from 39.7 ± 3.97 g/hr to 4103 ± 410 g/hr. The mean emissions measured were 1647 ± 165 g/hr which align with the arithmetic mean of Rella et al. (2015) – 1720 g/hr.

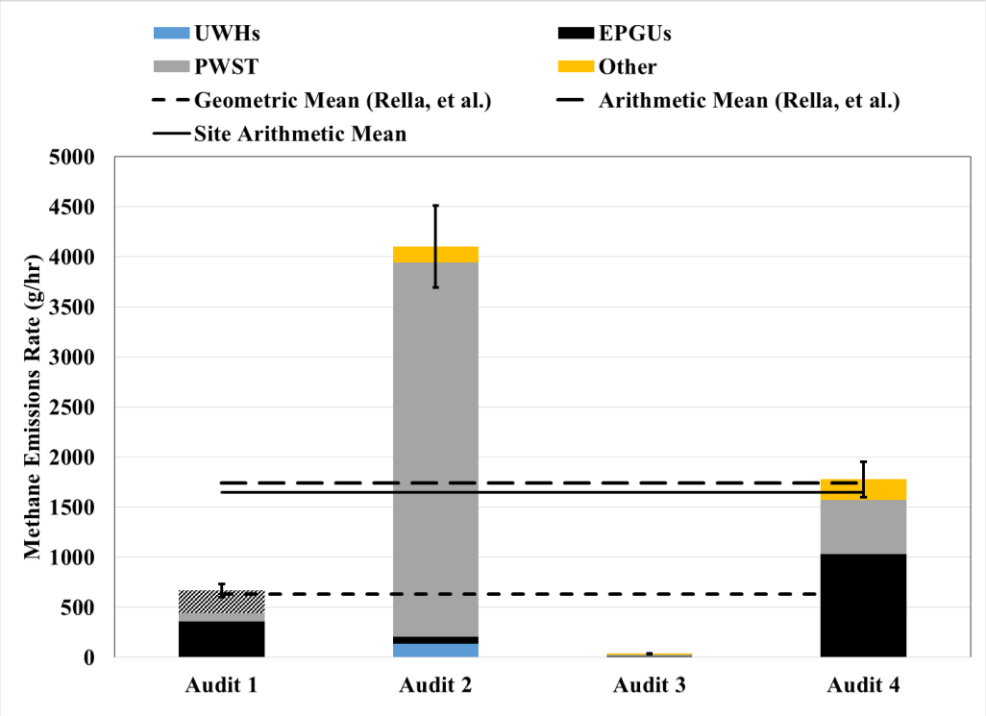

Figure 5.1: Combined audit results with the mean presented in comparison with data from literature.

Table 5.2 presents the total measured site emissions, total throughput and, relative loss rate for this unconventional well site. Using the audit data with corresponding NG production for those days, the relative losses ranged from 0.001 to 0.064% of the throughput. The mean loss rate was 0.029%. If the average methane emissions were used along with the total production over the 363 days the loss rate was 0.035%. The measurement uncertainty of methane is ±10%. The uncertainty in production reports is not known.

Conventional regression analysis showed the strongest correlation was between methane emissions and NG production. Production data was available on a daily basis and the total production of the site over these 363 days was 2,047 million cubic feet (MMCF). If this fit ere applied to daily NG production over the course of the year, the estimated methane emissions would be 7,818 kg/year. This would yield a loss rate of 0.019% which is about 35% lower than using the mean value.

Table 5.2: Methane emissions, throughput and relative losses. *kg/year, ^MMCF/year

	CH_4 Emissions	NG Production	Relative Loss
	kg/Day	MCF/Day	%
Audit 1	16.07	7224	0.011
Audit 2	98.49	7669	0.064
Audit 3	0.95	3154	0.001
Audit 4	42.67	9031	0.023
Mean	39.55	6769	0.029
Annual	14,355*	2040^	0.035

Products

Air

Presentation at ISES (International Society for Exposure Science), Raleigh, NC Oct. 16th, 2017 on "Techniques for Estimating Community Exposure from Hydraulic Fracturing Operations." (see attached powerpoint).

Vehicular

- NSF Proposal (with letter of support from NNE) – Submitted October 2017
- Presentation at Shale INSIGHT 2017
- Poster Presentation at AGU Fall Meeting 2017
- Draft Paper – Johnson, D., Heltzel, R., and Oliver, D., "Temporal Variations in Methane Emissions from an Unconventional Well Site," Geophysical Research Letter, Submitted December 2017.

Plan for Next Quarter

Air

The team will work on an invited paper titled "Dispersion of Traffic Related Ultrafine Particles in Complex Terrain" for The International Journal of Environmental Research and Public Health in a special issue concerning 'Transportation-Related Air Pollution and Human Health.' Due date of September 2018.

Vehicular

- Complete the fifth site audit.
- Currently working with LI-COR to purchase a reduce price analyzer using the additional funds that were recently released.
- Examine interest of "energy" audit for new well.

Topic 6 – Water Treatment

Approach

In this subtask, the Dr. Morrissey is characterizing the chemical and biological factors that influence radium accumulation in sludge from produced water. To accomplish this aim we are performing a series of laboratory microcosm experiments. Produced water is incubated in the laboratory with or without additions of sulfate and nutrients (C, N, P). The addition of nutrients is intended to stimulate the activity of microorganisms to immobilize sulfate and prevent it from precipitating with radium.

Results & Discussion

This is a new subtask, initially funded in September 2017. As such, activities in the fourth quarter of 2017 primarily consisted of establishing protocols, building microcosms, and preparing for the proposed experiments. The first experiments began in December 2017.

Microbial analysis of water samples from MIP 3H revealed the presence of halophilic bacteria and methanogenic archaea. Initial results from microcosm incubations indicate that precipitation of solids occurs primarily within the first seven days, additions of both sulfate and nutrients augment precipitate formation. Microbial activity is highest early in the incubation with rates of CO_2 and CH_4 production declining over time. Sulfate addition appears to reduce microbial activity while nutrient addition enhances microbial activity augmenting CO_2 but not CH_4 production. Water and sediment samples are being collected for analysis of Ra and other important chemical species (SO_4, Cl, Ba, Ca, Fe, Na, Sr). Chemical analysis will be completed within the first quarter of 2018.

Products

As this work is still in its early stages, there are no products to report for this quarter

Plan for Next Quarter

In the first quarter of 2018 the laboratory microcosm experiments will be completed. This will involve the completion of microbial and water chemistry analyses. When all data has been collected statistical analysis will be performed and results will be shared with the MSEEL team.

Topic 7 – Database Development

Approach

All MSEEL data is now online and available to researchers (Figure 7.1 and 7.2). The website has been updated with the latest production beyond the end of the quarter (Figure 7.3). Work continues

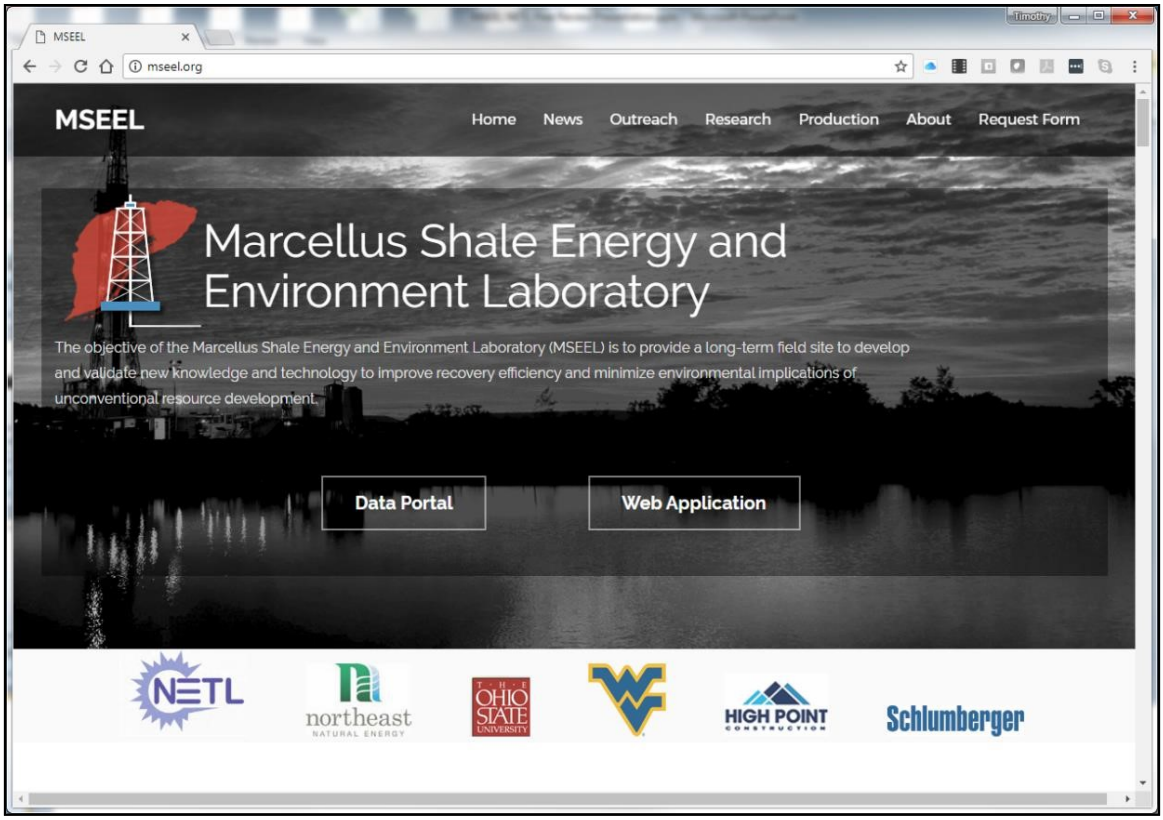

Figure 7.1: MSEEL website at http://mseel.org/.

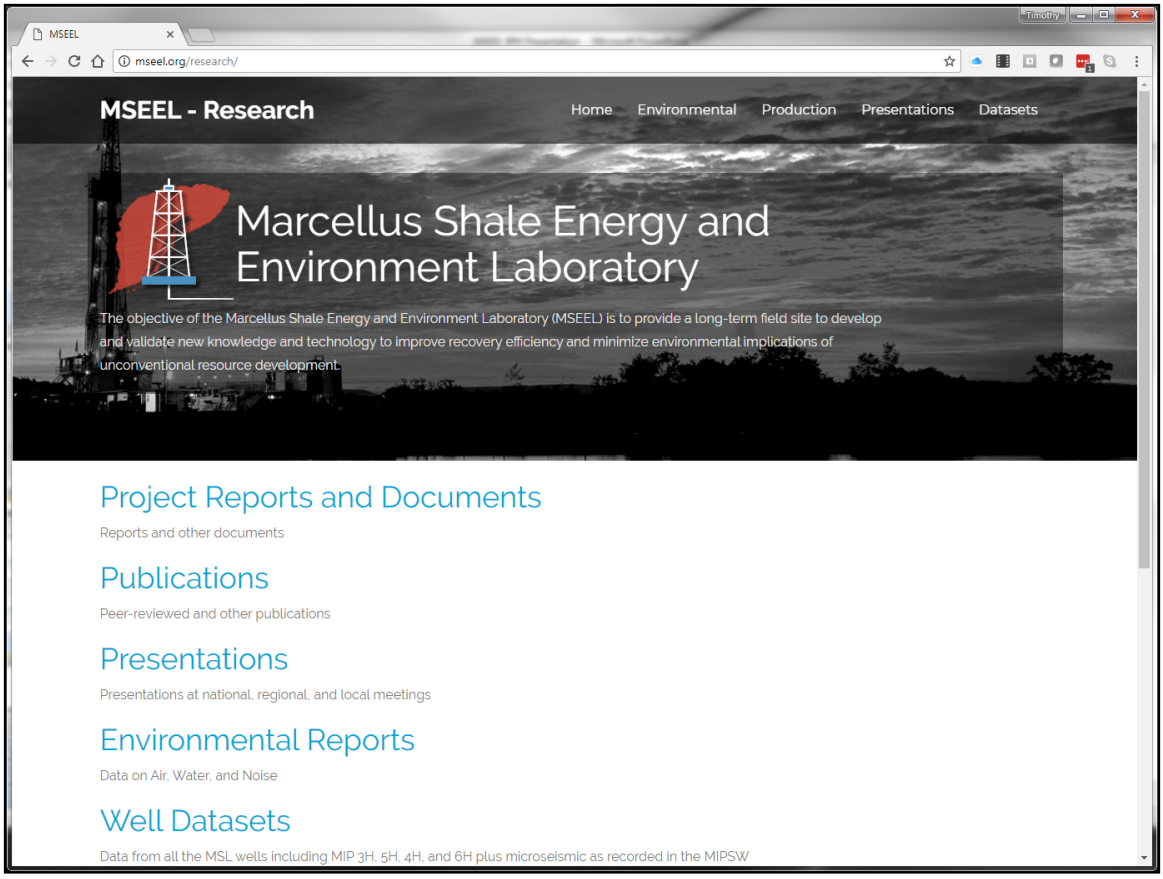

Figure 7.2: All data generated by the MSEEL project is available for download at http://mseel.org/.

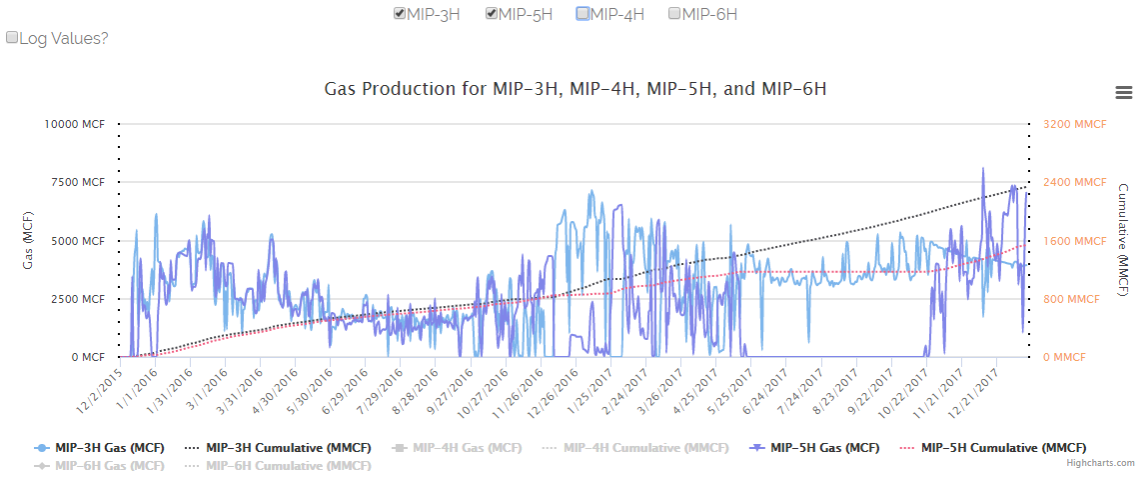

Figure 7.3: Gas and water production have been updated through the end of the quarter and are available at http://mseel.org/.

Results & Discussion

Data and publications are now available at http://mseel.org/.

Products

Web site enhanced and updated.

Plan for Next Quarter

Working to develop interactive programs to display user selected welllogs and geochemical data. A mock-up of the type of display is shown in Figure 7.4.

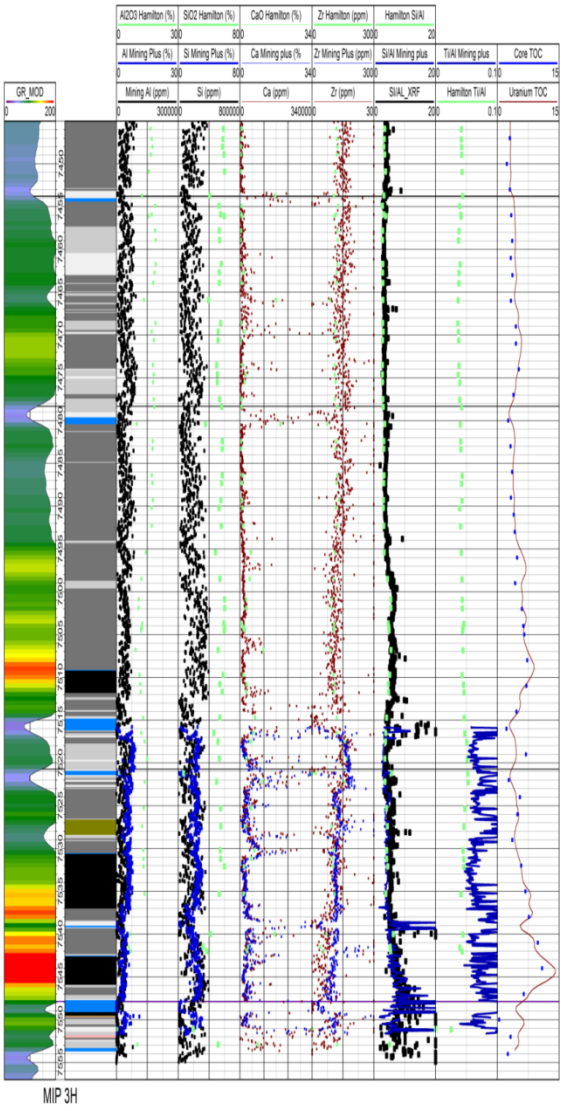

Figure 7.4: Mock up showing log and geochemical data for the MIP 3H pilot hole. The user will be able to select the type of data and scale of displays.

Topic 8 – Economic and Societal

This task is complete and will not be updated in future reports.

Appendix 1

SPESPE-189888-MS

Seismic Attribute Application for the Distributed Acoustic Sensing Data for the Marcellus Shale: A New Insights to Cross-Stage Flow Communication

Payam Kavousi Ghahfarokhi, West Virginia University
Timothy Carr, West Virginia University
Liaosha Song, West Virginia University
Priyavrat Shukla, Schlumberger
Piyush Pankaj, Schlumberger

This paper was prepared for presentation at the SPE Hydraulic Fracturing Technology Conference held in The Woodlands, TX, USA, 23-25 January 2018.

Abstract

Recently, oil and gas companies started to invest on fiber optic technology to remotely monitor subsurface response to stimulation. Distributed Acoustic Sensing (DAS) and Distributed Temperature Sensing (DTS) are two fiber technologies that record vibration and temperature around the fiber, respectively. In this research, we introduce new seismic attributes calculated from the DAS data that could suggest cross-stage fluid communication during hydraulic fracturing. The DAS data covers the entire 28 stimulated stages of the lateral MIP-3H well close to Morgantown, WV. We calculated the energy attribute for the DAS data of the studied stages. Subsequently, a Hilbert transform is applied to the DAS data to evaluate the instantaneous frequency of each trace in the DAS. In addition, we applied a Fast Fourier transform to each trace for all the SEGY files to calculate the dominant frequency with a 30 seconds temporal window. The dominant frequency is compared to the DTS data and energy attribute for the stages in the horizontal MIP-3H well. The DTS analysis shows that stimulation of the stages 10 causes a temperature rise in the previous stage 9; in contrast, stage 18 stimulation does not affect stage 17 temperature. We suggest that the common low frequency zone identified in instantaneous frequency and dominant frequency

attributes between stages 10 and 9 is related to presence of fluid that transferred cross-stage during hydraulic fracturing. The fluid results in the frequency damping of the vibrations around the fiber. We show that the frequency attribute reveals increases detail about the stimulation than conventional signal energy attribute of the DAS data.

Introduction

The multidisciplinary and multi-institutional team at Marcellus Shale Energy and Environmental Laboratory (MSEEL) work on geoscience, engineering, and environmental research in collaboration with Northeast Natural Energy LLC., several industrial partners, and the National Energy Technology Laboratory of the US Department of Energy. The purpose of this unique research is to develop and test new knowledge and technology to improve recovery efficiency while diminishing environmental implications of unconventional resource development. Before 2015, the two horizontal wells MIP-4H and MIP-6H were producing gas from the Marcellus Shale near Morgantown, West Virginia (Figure 1). Two other horizontal wells MIP-3H and MIP-5H were completed in 2015. Fiber optics technology including distributed acoustic sensing (DAS) and distributed temperature sensing (DTS) were deployed in the MIP-3H horizontal well near Morgantown, West Virginia to provide continuous subsurface vibration and temperature sampling during the stimulation. The MIP-3H stimulation over 28 stages involved injection, at high pressure, averaging 8500 psi (58.6 MPa), to break the formation and establish a complex network of permeable fracture pathways.

Figure 4: Marcellus Shale Energy and Environment Laboratory (MSEEL) just outside Morgantown, West Virginia, USA. The MSEEL site consists of four horizontal production wells operated by Northeast Natural Energy LLC. (MIP-3H, MIP-4H, MIP-5H, MIP-6H), two pilot holes (MIP-3 and MIP-4), and a micro-seismic and sampled observation well (MIP-SW), and a grid of five surface seismometer (triangles).

The first well in the Marcellus shale was completed in Oct 2004. In 2005, all horizontal wells drilled in Pennsylvalia were conventional wells. Since the end of 2008 there was a surge in horizontal well drilling activity in the Marcellus shale which peaked in 2013 and 2014 (Beckwith,

2013), and with that came widespread hydraulic fracturing. During hydraulic fracturing, large quantities of fluids are pumped to create the fracture followed by proppant to hold the fracture open. With time, operators have evolved their completion designs and pumped bigger job sizes to improve production performance. Average lateral lengths increased from 4,000 ft to 6,000 ft and proppant volumes more than doubled between 2010 to 2014 (Kugler et al. 2015). The fracture connects to the matrix and provides a large surface area and conductive pathway for fluids to flow from matrix to the wellbore. Therefore, more than fracture conductivity, matrix deliverability plays a critical role in production from unconventional reservoirs (Economides et al., 2000). Uncontrollable fractors like geology and reservoir quality also play a dominant role in the success of a well. Neural network models developed on 48 Marcellus wells concluded that gas production is proportional to depth, thickness and hydrocarbon maturity (Shelley et al., 2014). However, controllable factors like completion quality also play an important role. Operators have used engineered completion designs, which place perforation clusters in similarly stressed areas to achieve uniform stimulation along the wellbore. Such completions have increased the EUR in Marcellus shale wells by 30% in some cases (Walker et al., 2012). Researchers have also analyzed channel fracs, a technique to create highly conductive fractures, and its applicability to Marcellus shale (Ajayi et al., 2011).

Natural fracture presence plays an important role in production performance of shale wells by creating a complex fracture network during hydraulic fracturing. Outcrop analysis, image logs, caliper logs, regional stress trends and seismic ant tracking are some of the methods used in mapping natural fractures. Stochastic methods are commonly used to create a distribution of natural fractures based on their intensity. During the fracturing operation, natural fractures can also lead to cross stage communication which can be sensed using fiber optic technology as discussed in this paper. The ultimate success of hydraulic fracturing is known only by the production results, but diagnostic methods help to understand the performance of a fracturing job in real time.

Traditionally, surface pressure and subsurface pressure gauges, well head rates, and radioactive traces are the only monitoring tool for completion engineers during the hydraulic fracturing (Mollennar, 2012). Shallow depth of investigation limits the application of the traditional techniques in complex reservoirs (Mollennar et al., 2012). The need for more robust diagnostic tools encouraged the oil and gas companies for using fiber-optic technology. Fiber-optic sensing technology has been applied to the oil and gas reservoirs from 1990s to monitor steam injection, injection profiling, acid injection profiling, and hydraulic fracture diagnostics (Karaman et al., 1996; Rahman et al., 2011; Glasbergen et al., 2010; Sierra et al., 2008; Holly and Kalia, 2015). The early application of the fiber-optic technology was Distributed Acoustic Sensing (DTS), which was only able to record the temperature. DTS is still widely used for unconventional oil and gas reservoir to monitor the temperature in the subsurface during stimulation, production, or injection. Distributed acoustic sensing (DAS) technology was later introduced to the industry to perform more robust diagnostics of the subsurface (Molenaar et al., 2012). It was originally developed in defense industry, and has become more popular in the oil and gas industry with application from completion to production to abandonment. DAS or distributed vibration sensing (DVS) uses optical fibers to measure the dynamic strain at all points along the fiber (Parker et al, 2014). These remote sensing techniques have provided unparalleled acoustic sampling from the subsurface during hydraulic fracturing. A single silica fiber with protective jacket is clamped to the outer part of the production casing (Figure 2).

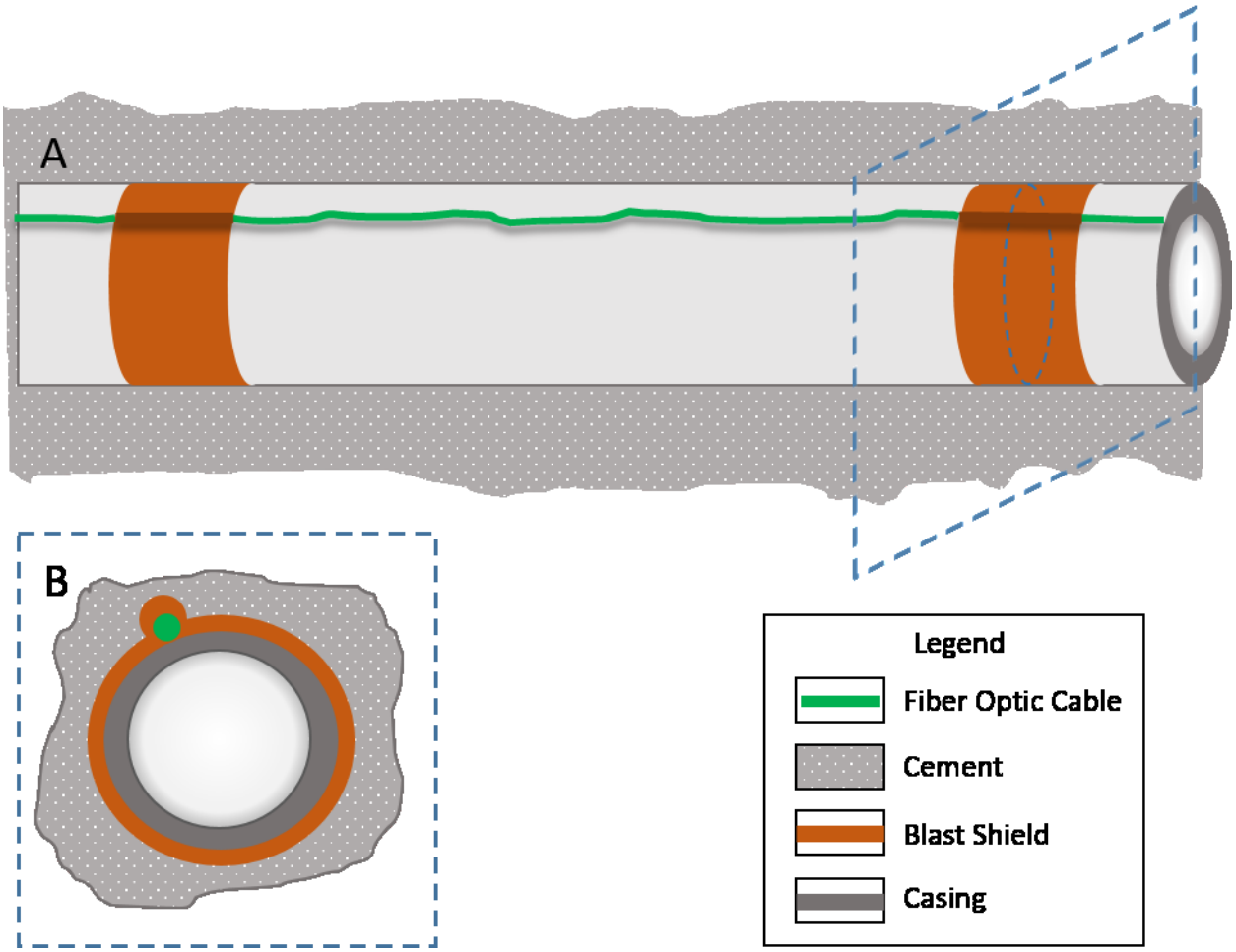

Figure 5: Schematic depiction of the fiber-optic-cable installation. (A), the cable is attached to the outer part of the production casing and sorrunded by the cement, notice the cable is not straight. (B), profile view of cable installation. The location of the profile is illustrated in (A) with dash lines. Image is not up to scale.

This permanent in-well fiber brings the possibility of time-lapsed measurements and monitoring without well intervention and production deferment. The first field application of DAS was undertaken by Shell Candada during the completion of a tight gas well in February 2009 to optimize the treatment (Mestayer et al., 2011; Molenaar et al., 2012). The DAS technology has also been utilized for the Vertical Seismic Profiling (VSP) as a replacement for geophones (Miller et al., 2012; Bakku et al., 2014; Mateeva et al.,2012; Mateeva et al., 2013; Madsen et al., 2013). Webster et al., (2013) used DAS to detect microseismic events and verified their results with geophones in the borehole.

DAS technology has provided a more real-time tool for hydraulic fracturing monitoring without well intervention (Mollennar et al., 2012; Mollennar and Cox, 2013; Bakku et al, 2014; MacPhail et al., 2012). Unlike traditional hydraulic fracturing monitoring techniques that requires movement of the acquisition system for each stage stimulation, DAS uses a fiber that can be permanently attached to the production casing. Thus, it removes the time delay of several hours and facilitates decision making for completion engineers.

Boone et al., (2015) showed that DAS can be used to characterize perforating gun signature to measure the zero timing of the perf detonation down to microseconds. For cemented plug and perf (CPnP) completions, an optimal hydraulic fracturing depends on proper seating of plug and the ball on it to isolate the perforated casing from the completion below. The ball seating on the plug generates a strong signature on the DAS (Boone et al., 2015).

The DAS senses the vibration in the local environment around the fiber and provides a measure of the relative strain of the optical fiber. The technology is based on the optical time domain reflectometry (OTDR). OTDR systems include a laser light transmitter and an optical detector. High power laser transmitter sends an accurately timed light down the sensing fiber; because of impurities inherent in the glass core, the lights are scattered back to the detector. A tiny fraction (<0.000001%) of the forward propagating pulse backscatters toward the detector as the pulse travels through the fiber. Measuring the power and the wavelength of the backscattered light enables the detector to estimate the temperature, strain, or the vibro-acoustic on the fiber (Tanimola and Hill, 2009). Any incident angle above the critical angle results in light refraction and hence dissipation in the surroundings.

The time delay and the amplitude of the backscattered wave is used by the OTDR detector to calculate the point at which backscattering is happened. A fiber optic can be assumed as a series of tiny mirrors joined together; any movement of these mirrors modify the backscattered waves, which can be measured (Kimble, 2013). Changes of physical environment around the fiber such as temperature, dynamic strain, and vibro-acoustic disturbance alter the mirror's reflective characteristics (Kimble, 2013). The sensitivity of the fiber to the vibro-acoustic waves around it will convert the entire fiber to an array of microphones that can detect vibrations around the fiber. The DAS data is usually processed as series of hearing devices using a gauge length parameter (Figure 3). The DAS detector unit (interrogation unit) send consecutive light pulses into the fiber, the backscattered signal of the first pulse are S1 and S2; the second emitted pulse get backscattered as S1' and S2' from the begining and end of the gauge length, respectively (Figure 3). By measuring the phase lag between the backscattered signals from the two end-points of the gauge lengths, the relative strain can be relatively estimated (Li et al., 2015). The backscattered pulse can be processed every 100μsec corresponding to a 10 kHz sampling rate. These parameters can be adjusted to optimize the performance of the operation (Mollennar and Cox, 2013). DAS continuously process the phase lags of the backscattered; However, simultaneous processing of backscattered is limited to 40,960 sensing points. This limitation brings the receiver spacing between 1 to 10 meters (Conway and Mondanos, 2015).

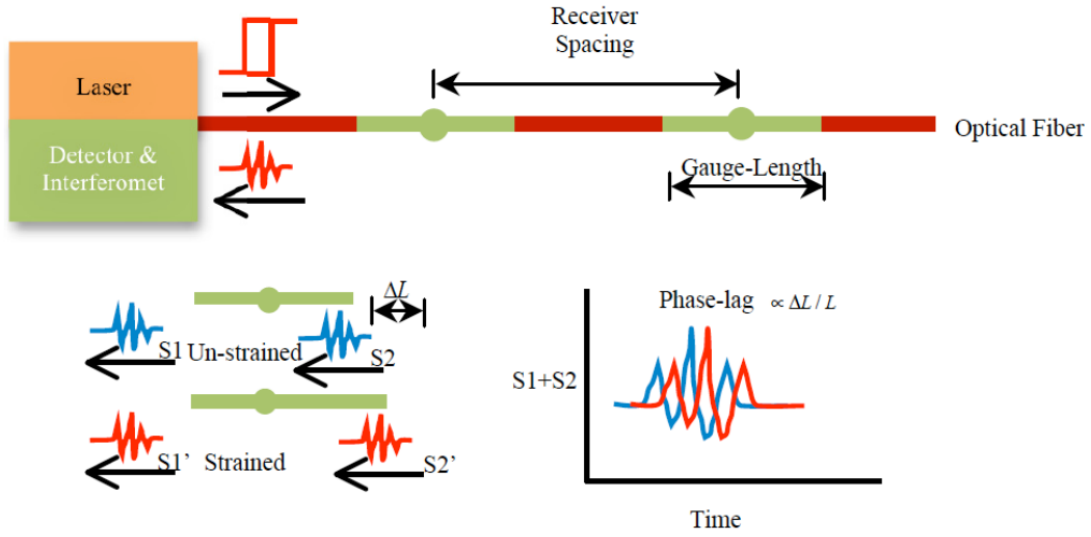

Figure 6: DAS measurements principle. (S1+S2) represents the sum of the backscattered signals from the front and the end of the gauge length in un-strained fiber for the first emitted pulse. (S1'+S2') is the sum of the backscattered signals of the second emitted pulse. The backscattered signals are from the front and the end of the gauge length after the fiber is deformed. The phase lag between (S1+S2) and (S1'+S2') is proportional to the fiber stain. Courtesy of Li et al., (2015).

The distributed temperature sensing (DTS) data can also be recorded from the same fiber deployed to the well. The temperature can be estimated from the backscattered light spectrum. DTS technology measures the "Stokes" and "Anti-Stokes" components of the backscattered spectrum (Figure 4). The "Anti-Stokes" component is sensitive to the temperature, while the stoke component is temperature independent. Thus, a ratio of "Anti-Stokes" and "Stoke" power could provide a measure for the temperature (Molenaar et al., 2012).

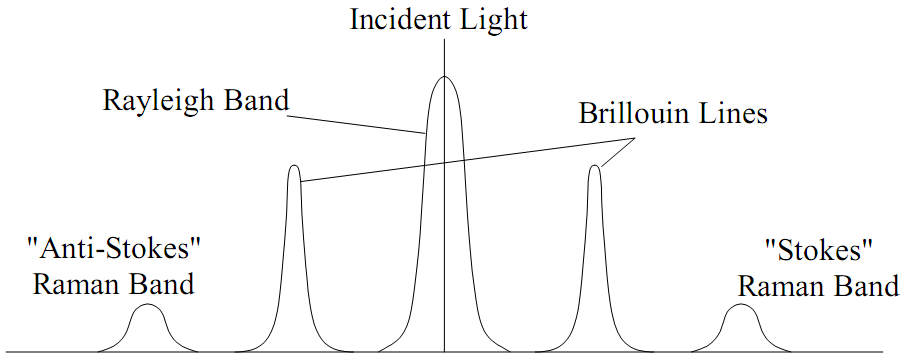

Figure 7: The backscatted light spectrum has Rayleigh Band, Brillouin bans, and Raman bands. Rayleigh band are sensitive to strain while Raman band are sensitive to the temperature around the fiber (courtesy Carnahan et al.,1999)

Geologic background

The Marcellus Shale spans 95,000 square miles (246,000km^2) across six states in northeastern U.S., which makes it the most extensive shale-gas play in North America (Carr et al., 2011; Wang

and Carr, 2013). Marcellus Shale is in the lower portion of Hamilton Group, middle Devonian, and it is covered by Tully Limestone and Mahantango Formation. Cherry Valley Limestone divided the Upper and Lower Marcellus Shale (Figure 5). The Marcellus Shale is a distal marine mudstone within a westward-prograding foreland succession deposited in the Appalachian basin, which represents a periodically deepening basin tied to tectonics during the Acadian orogeny (Ettensohn, 1985; Lash and Engelder, 2011, Zagorski et al., 2012; Carr et al., 2013; Milliken et al., 2013; Song et al., 2017). Dominant marine medium-gray to gray burrowed mudstone interbedded with silty mudstone, siltstone, and sandstone intervals are interpreted to reflect regional shallowing, and finely laminated, dark gray to black, organic-rich mudstone, commonly associated with thin beds of skeletal carbonate are interpreted to reflect relative deepening (Ettensohn, 1985; Ettensohn et al., 1988). Ettensohn 1985 and Ettensohn et al., 1988 ascribe these deepening events to a tectono-stratigraphic model. However, Sageman et al., 2003 presented an oscillating seasonal dysoxia – anoxia model, and argued that relative sea-level, a combination of tectonic subsidence and eustasy, is the controlling factor. The Marcellus Shale has recently attracted great attention as an important gas-producing unit (Engelder and Lash, 2008; Zagorski et al., 2012). The paleogeography from the Middle Devonian shows that Well MIP-3H is located in the middle of the basin (Figure 6). The well MIP-3H is drilled just above the Cherry Valley Limestone in the Upper Marcellus Shale (Figure 7).

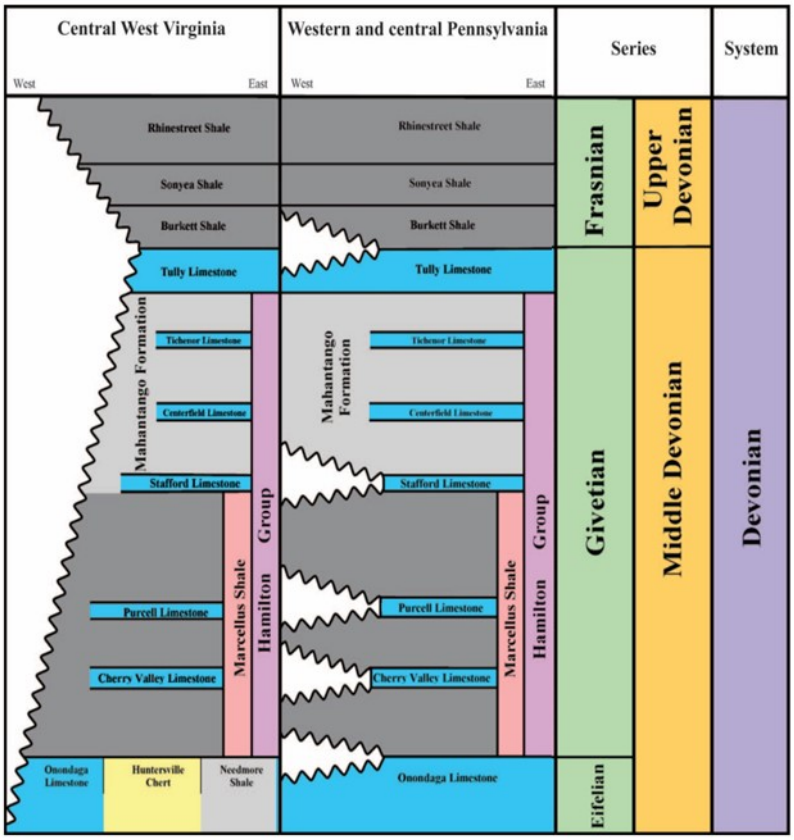

Figure 8: Middle Devonian stratigraphy in West Virginia and Pennsylvania (from Zagorski et al., 2012).

Figure 9: Reconstruction of Middle Devonian paleogeography (from Blakey, 2010). The study well (MIP-3H) is in the middle of the basin.

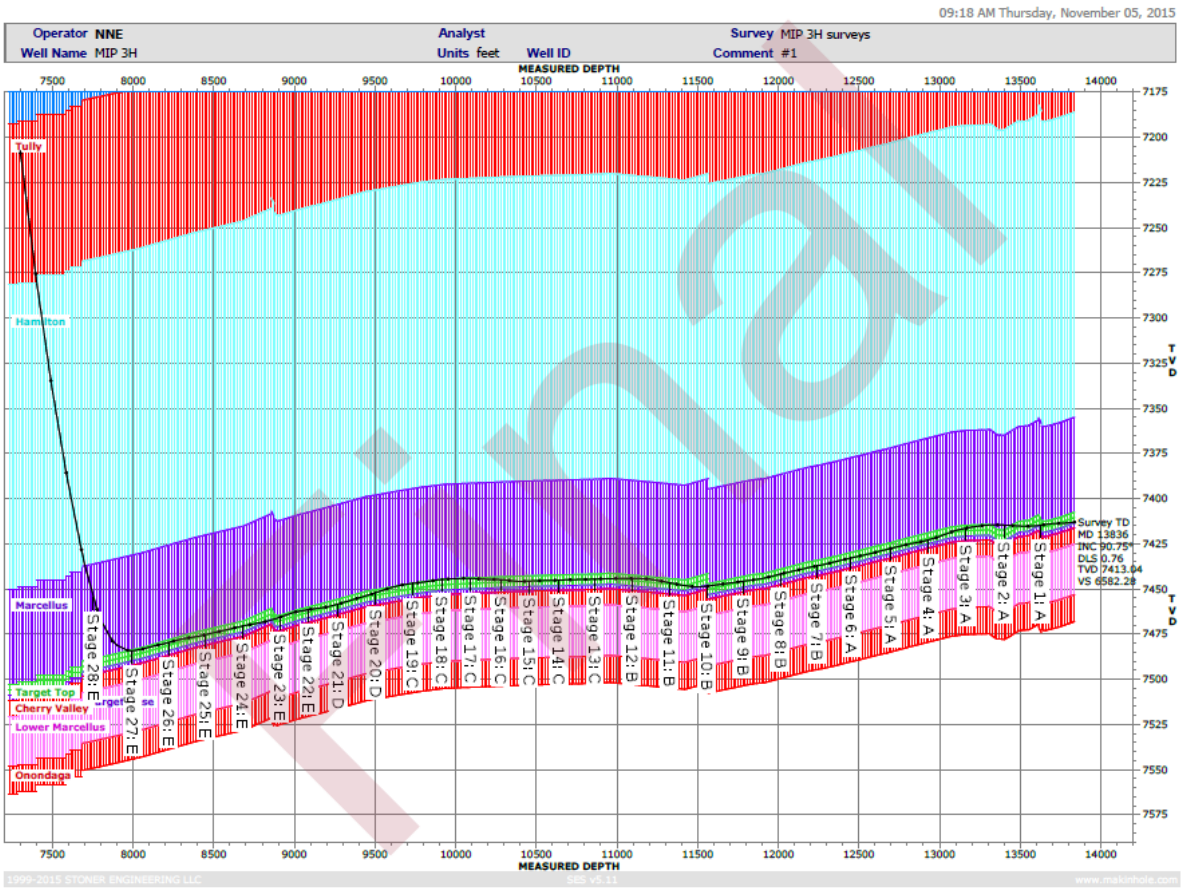

Figure 10: The MIP-3H lateral was kept above the Cherry Valley Limestone in the Upper Marcellus Shale.

Methodology

The DAS data are in binary format and recorded as SEGY files for every 30 seconds of the stimulation job. The SEGY file is comprised of 493 traces and 200 to 300 SEGY files typically encompass a moderate sized 2-3 hours stimulation. The DAS data covers the entire 28 stages of the lateral MIP-3H. Figure 8 shows a single 30 seconds SEGY file recorded during the stimulation of the stage 14 of MIP-3H well. The SEGY file has 493 traces with 60,000 samples per trace. This is equivalent to sampling rate of 0.5 msec. Seismic attributes are widely used to extract information such as frequency, amplitude, attenuation, etc. from seismic traces. We show that these attributes can also be employed for distributed acoustic sensing data to extract more subtle information than common energy attribute about the hydraulic fracturing process, specially the cross-stage flow communications.

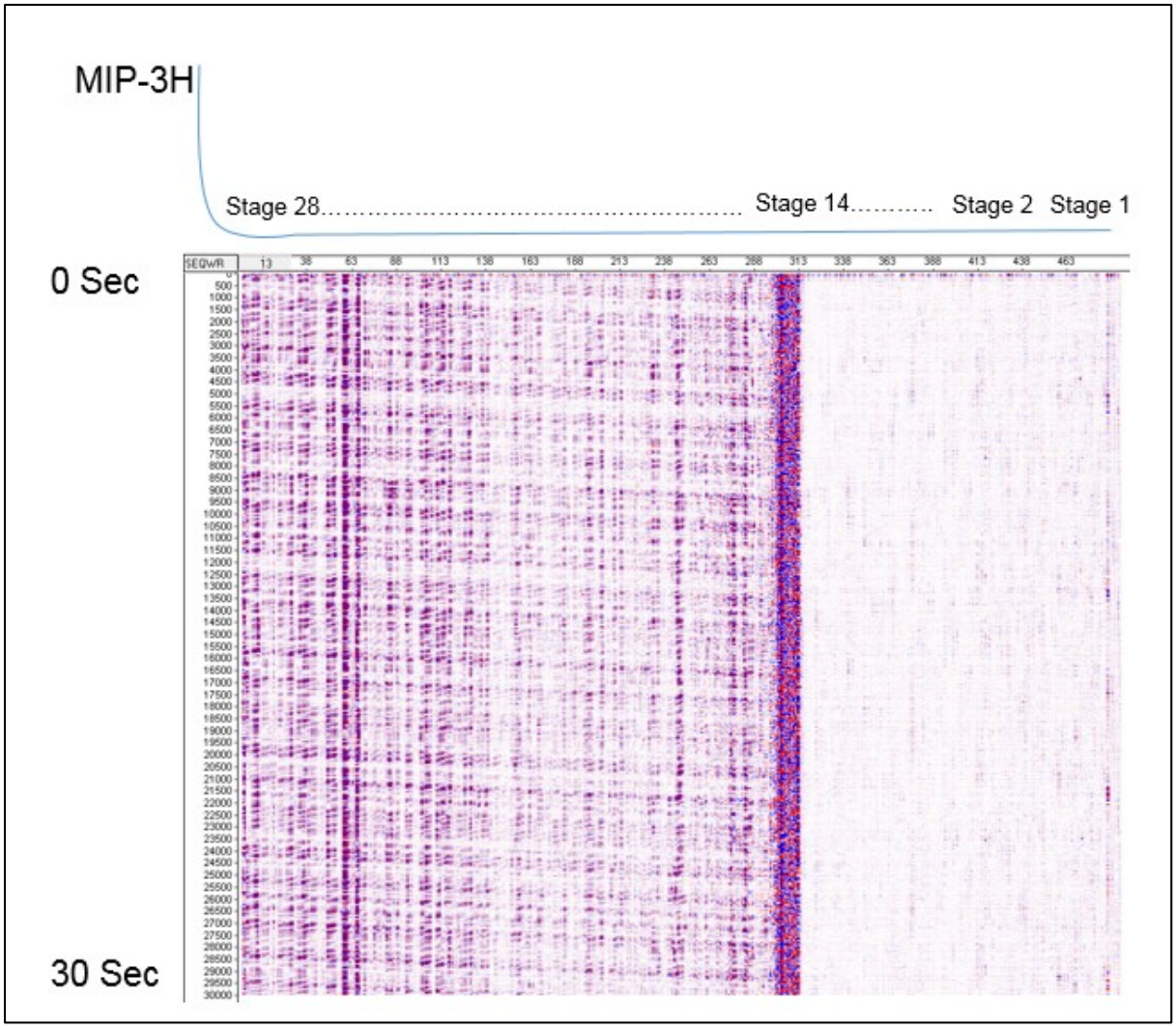

Figure 11: A single 30 seconds SEGY file recorded during the stimulation of the stage 14 of MIP-3H well. Minimal vibrations are recorded for stage 1 to stage 13 because these stages were separated from stage 14 to stage 28 by a plug.

We applied several common seismic attributes to the DAS data. These attributes include energy, instantaneous attributes, and dominant frequency. The computations are conveyed through an in-house processing software developed in the MSEEL research group at West Virginia University.

Energy Attribute: The energy of a discrete signal can be calculated as:

$$E = \sum_{n=-\infty}^{\infty} |x(n)|^2 \qquad Eq.1$$

Each SEGY file has 493 traces and 60,000 samples. We calculate an energy attribute with a 30 seconds temporal window. The energy attribute for a SEGY file can be calculated as (Kavousi et al., 2017):

$$E_{ik} = \sum_{j=1}^{60,000} x_k(j)^2 \quad i = 1 \dots 493, k$$
$$= 1 \dots Number\ of\ the\ SEGY\ files \qquad Eq.2$$

Where $x_k(j)$ is sample j from 60,000 samples in trace i from k^{th} SEGY file. Thus, there are 493 energy values calculated for every time step of 30 seconds during the fracture stimulation for each SEGY file.

Instantaneous attributes: A seismic trace can be assumed as a projection of an analytic signal (complex signal) on the real domain. Attributes such as instantaneous frequency, instantaneous phase, and instantaneous amplitude can be calculated at any sample of the trace using the analytic complex signal. Complex traces were introduced to reflection seismology in early 70's and later followed by instantaneous attribute traces for seismic analysis (White, 1991). A complex trace separates phase from amplitude and then allows calculation of instantaneous attributes (Zhang and Bentley, 2000). Complex trace analysis has been applied to geophysical data processing by Barnes (1990, 1991, 1992 and 1993), Bodine (1984), Farnbach (1975), Ha et al., (1991), Robertson et al., (1984 and 1988), Taner et al., (1977 and 1979) and White (1991). The instantaneous attributes are available through most of the seismic interpretation workstations. These attributes describe the waveform shape of the seismic trace. The two basic instantaneous attributes are instantaneous amplitude and instantaneous phase. Instantaneous frequency is the differential of instantaneous phase. The analytic signal can be assumed as a spring, the more contracted the spring, the higher the instantaneous frequencies (Figure 9). The imaginary part of the analytic signal is called quadrature trace, which can be found by a 90° phase shift to the real signal. A peak or a through in the real signal corresponds to a zero-crossing in the imaginary signal, and vice versa. The imaginary signal can be calculate using a Hilbert transform.

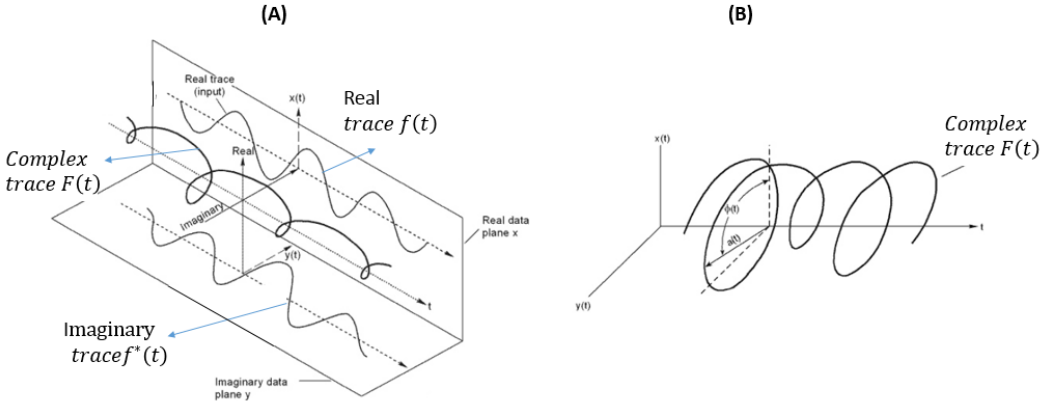

Figure 12: (A) The real trace is the projection of the complex trace on the real plane. The imaginary trace is the Hilbert transform of the real Trace. (B) The $a(t)$ is the vector perpendicular to the time axis which connects it to the complex trace, its length is referred as the instantaneous amplitude at time t. $\theta(t)$, the instantaneous phase, is the angle that vector $a(t)$ makes with the vertical axis at time (t) (Modified from Hardage, 2010).

Seismic data transformation is often used to extract information about the waveform that are not visible in the real domain amplitude-time data. One of the most common transformation of time series is the Fourier transform which takes time series (seismic data) to the frequency domain. Fourier transform allows the evaluation of the frequency content of a portion of seismic trace;

however, it does not provide local measurement of the frequency for example at 1 sample in the seismic trace (Taner et al., 1977). Other transformation such as Hilbert transform can be used to calculate the analytic (complex) signal for instantaneous amplitude and instantaneous phase evaluations. The latter two attributes are the basis for evaluating instantaneous frequency at each sample of the seismic trace. Complex signal calculation for the seismic data was introduced by Taner et al., (1977). A seismic trace $f(t)$ can be considered as the real part of a complex trace (Figure 9):

$$F(t) = f(t) + if^*(t) \qquad Eq.3$$

where $f^*(t)$ is the imaginary signal (quadrature signal) calculated by a 90° phase shift of the real signal using a Hilbert transform. The real trace $f(t)$ can be expressed as a time-dependent amplitude $A(t)$ and a time dependent phase $\theta(t)$ as (Taner, 1977):

$$f(t) = A(t)\cos\theta(t) \qquad Eq.4$$

The quadrature signal then has a 90° phase shift relative to the real trace:

$$f^*(t) = A(t)\sin\theta(t) \qquad Eq.5$$

And the complex trace is:

$$F(t) = f(t) + jf^*(t) = A(t)e^{i\theta(t)} \qquad Eq.6$$

Knowing the $f^*(t)$ and $f(t)$, we can find $A(t)$ and $\theta(t)$:

$$A(t) = \sqrt{f^2(t) + f^{*2}(t)} = |F(t)| \qquad Eq.7$$

And

$$\theta(t) = \tan^{-1}[f^*(t)/f(t)] \qquad Eq.8$$

$A(t)$ and $\theta(t)$ are instantaneous amplitude (trace envelope) and instantaneous phase of the complex trace, respectively. Then, the instantaneous frequency can be calculated as the derivative of the instantaneous phase:

$$\omega(t) = \frac{d}{d(t)}\{\tan^{-1}[f^*(t)/f(t)]\} = \frac{f(t)\frac{df^*(t)}{dt} + f^*(t)\frac{df(t)}{dt}}{f^2(t) + f^{*2}(t)} \qquad Eq.9$$

The empirical observations suggested that there is a shift toward low frequency zones below gas sands (Taner, 1977). Rocks that are saturated with oil and gas cause the high frequency attenuation. Tai (2009) undertook a time-frequency analysis and showed that gas saturated sands are associated with a low frequency zones. One possible explanation would be the damping effect of the gas sands that filters out the higher frequencies. We propose the similar idea for the distributed acoustic sensing (DAS) data; when the fiber is surrounded by higher saturation of fluid, its vibration is dampened relatively fast and high frequencies are attenuated. Thus, the spectrum of the DAS signals shifts toward lower frequencies. As an analogy, a spring that is oscillating in a viscous fluid dies faster (i.e. higher frequency oscillations get attenuated faster) than a spring oscillating in the air. This phenomenon is referred as an "overdamped" oscillation in the engineering literatures (Alciatore, 2007; Rao and Qiu,1993).

Dominant Frequency: Fourier transform shows the similarity between various frequencies sinusoids and the seismic trace (Barnes, 1998). Frequency analysis deals with frequency contents of each 1D trace at the time domain. It transforms each 1D signal into the frequency domain by means of frequency decomposition algorithms such as Fast Fourier Transform. For length N input trace x, the discrete Fourier transform (DFT) is a length N trace X, with elements:

$$X(k) = \sum_{n=1}^{N} x(n) e^{\left(\frac{-2\pi i(k-1)(n-1)}{N}\right)} \qquad 1 \leq k \leq N \qquad Eq.10$$

Frequency analysis has been extensively carried out to find time varying spectral properties of seismic data (Barnes, 1993). Three average parameters are usually used to characterize a frequency spectra: the center frequency, the spectral bandwidth, and the dominant frequency (Widess, 1982; Kallweit and Wood, 1982; Berkhout, 1984). The average frequency of the power spectrum is referred as central frequency, and the standard deviation around the central frequency is defined as the spectral bandwidth (Figure 10) (Berkhout, 1984). The dominant frequency is the density of amplitude maxima in the power spectrum (Kallweit and Wood, 1982; Widess, 1982; Yilmaz, 1987; Sheriff, 1995). The second moment of the power spectrum is also equivalent to the dominant frequency (Barnes, 1993).

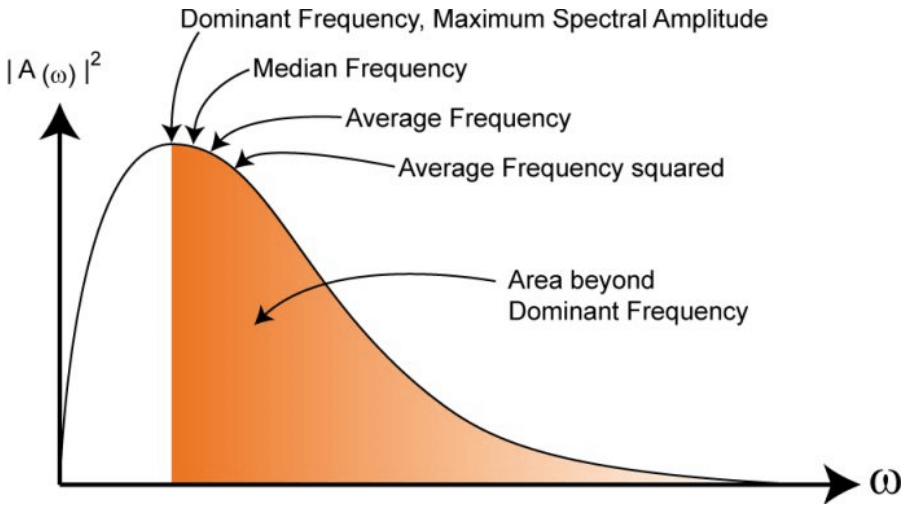

Figure 13: The frequency attributes that can be calculated from the spectrum resulted from Eq.10 (OpendTect Documentation).

We applied a Fast Fourier Transform to each trace for all the 220 SEGY files to calculate the dominant frequency with a 30 seconds temporal window. The dominant frequency is compared to the DTS data and energy attribute for stage 10 and stage 18 stimulation in the MIP-3H well. We propose that damping effect is also detectable in dominant frequency attribute. Higher frequencies are attenuated when the fiber is surrounded by the gasy fluid. Hence, low dominant frequency zones are evident.

Results and Discussions

We calculated the energy, instantaneous frequency, and dominant frequency attributes for several stimulated stages in MIP-3H lateral. One common way to visualize the DAS data is to use a waterfall plot; it has the measured depth of the well in the vertical axis and number of the timesteps in the horizontal axis. The color shows the calculated attribute for that timestep.

Figure 11 is the calculated energy attribute for stage18 in MIP-3H. 220 SEGY files form 220 timesteps of 30 seconds for 493 traces. Usually the visualization window will be limited to the zone of the interest around the stimulated stage (Figure 11).

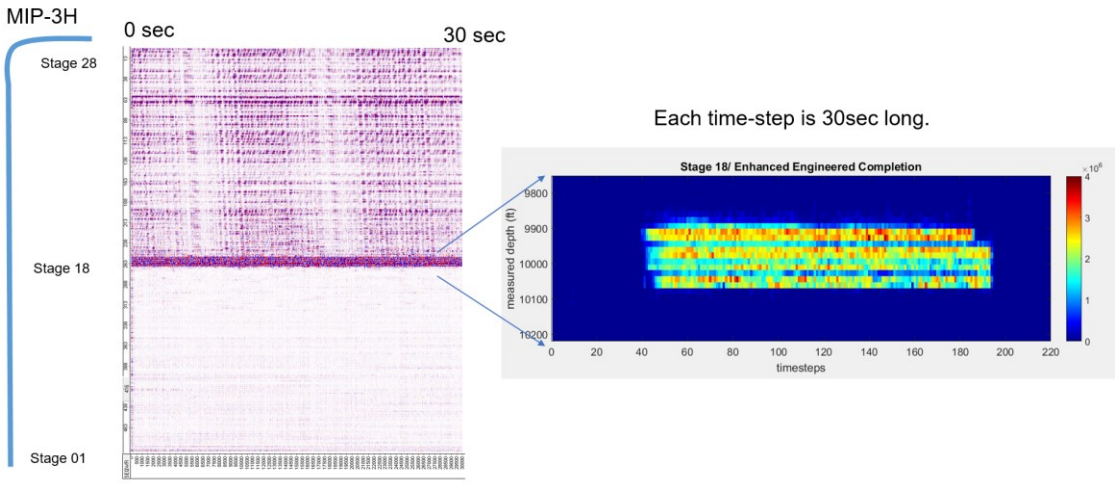

Figure 14: The energy attribute is evaluated for the stage 18 in MIP-3H well. The Eq.2 is used to calculate the energy attribute for the traces in vicinity of the stage 18 for 220 SEGY files (i.e. 110 minutes stimulation job).

In this study, we focus on stage 10 attribute analysis. Firstly, the instantaneous frequency and the amplitude of the DAS data are calculated for every 0.5 millisecond (Sampling rate of the DAS data). Figure 12 shows local low frequency zones in stage 9 during stage 10 stimulation. DAS amplitude does not reveal significant energy for stage 9. The plug and perf mechanism is employed for the completion of the MIP-3H. This procedure seals the direct connections between stage 10 and stage 9 through the wellbore. Stimulation of the stage 9 took place around 2 hours before stage 10 stimulation. The fracturing fluid of stage 9 rested at the formation and got warmed to almost the reservoir temperature of 160 °F. Subsequent stimulation of stage 10 pushed the warmed gasy fluid of stage 9 back toward the well through fractures and faults and hence a temperature rise is observed. High fracture intensity close to the base of the stage 10 and top of the stage 9 are observed in the wireline image logs (Figure 12).

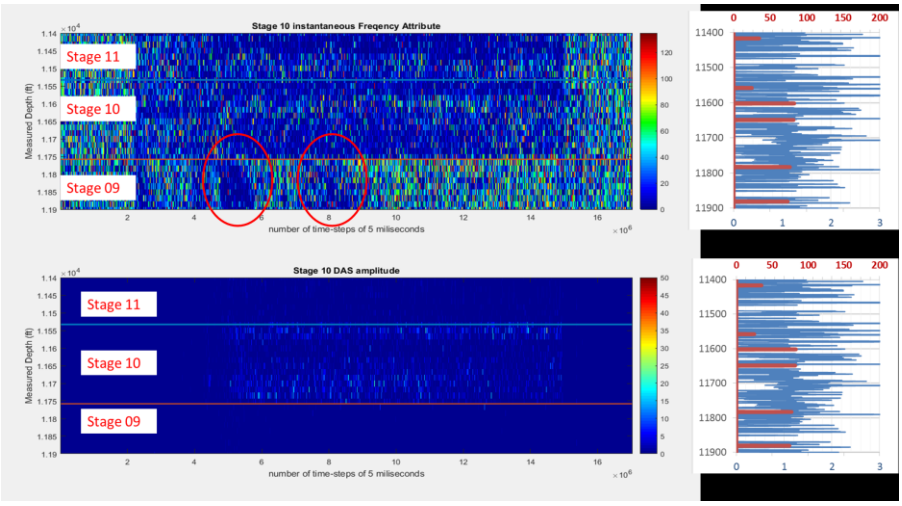

Figure 15: Instantaneous frequency shows that the stimulation of the stage 10 results in low frequency zones in stage 9 while the vibration amplitude does not reveal any vibration. The blue bars in the histograms on the right of the waterfall plots show the fracture intensity at each depth.

In addition to the DAS data, the DTS data are also recorded during the stage 10 stimulation. DTS shows that the temperature is raised in stage 9 while fracturing stage 10 (Figure 13). Amini et al., 2017 and Carr et al., 2017 noticed this temperature rise for several other stages in MIP-3H. They

suggested that numerous fractures and faults close to the stage boundaries are possibly responsible for this abnormal observation.

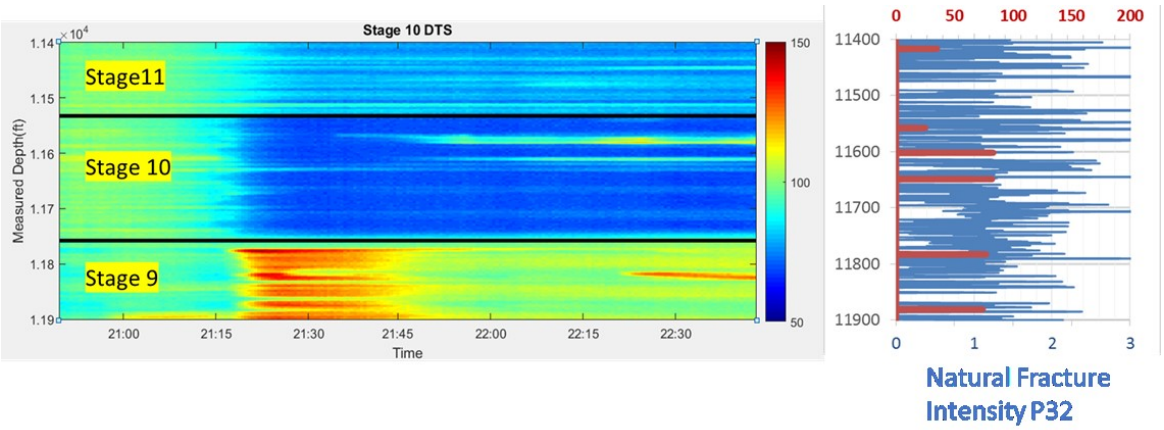

Figure 16: The stage 10 stimulation increased the stage 9 temperature. Note the high fracture intensity at the upper part of the stage 9.

Wilson et al., (2016) studied the natural fractures in the MIP-3H lateral and MIP-3H Pilot well (the vertical well) and extracted the trends of the natural fractures. A single fracture set oriented in N79°E was observed in the MIP-3H. The image logs from the vertical MIP-3H Pilot showed two set of fractures: an open fracture set oriented in N57°E and a healed fracture set in N87°E (Figure 14).

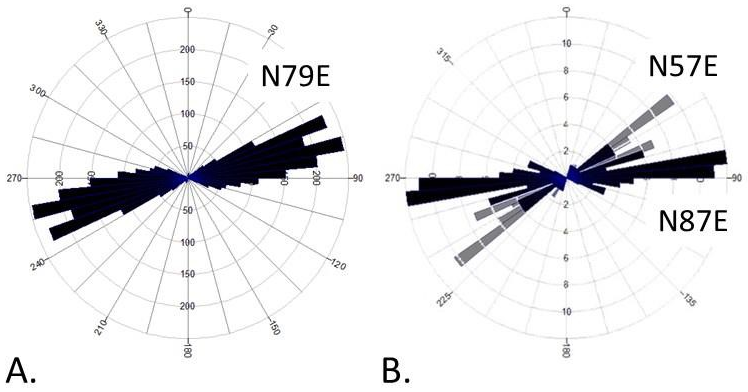

Figure 17: Rose diagrams of natural fractures a) observed along the length of the MIP-3H lateral (N=1640) and B) in the vertical pilot well (N=91). Fractures observed in the vertical well consist of 21 open fractures (light grey color) in the N57°E cluster and 70 healed fractures mainly concentrated in the N87°E cluster with a smaller fraction falling in the N57°E cluster. (Courtesy of Wilson et al.,2017)

Carr et al., (2017) used the interpreted fractures orientation from both MIP-3H and MIP-3H Pilot and proposed a conceptual model to explain the temperature rise in stage 9, during stimulation of the stage 10 (Figure 15). The conceptual model has two pre-existing natural fracture sets oriented at N79°E and N57°E. MIP-3H is oriented in N36°W; hence, hydraulic fractures could form along non-critically oriented N79°E preexisting fractures in the lower Marcellus Shale as aseismic "slow slip" not detected by standard microseismic monitoring. The oblique orientation of the lateral well to the preexisting fractures could explain the warming as detected by DTS of stage 9 to near formation temperatures by movement of fluids previously injected and warmed by the formation through stimulated fractures communicating from stage 10 to stage 9.

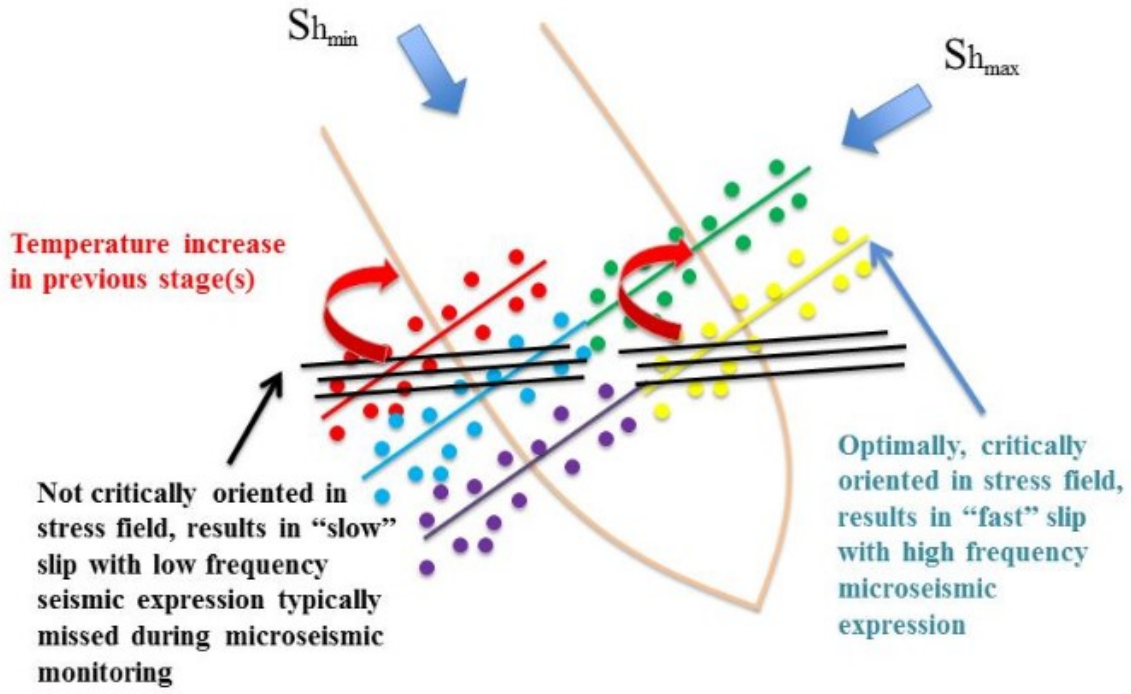

Figure 18: Conceptual model of observed pattern of the numerous preexisting N87°E fractures and faults observed in logs, microseismic orientated N59°E, LPLD events and warming observed in DTS in previous stages during fracture stimulation in the MIP-3H. Basic figure was modified from Das and Zoback, 2012. Movement and injection along non-critically oriented preexisting fractures in the lower Marcellus Shale resulted in the "slow" slip with low frequency seismic expression that was not picked up by microseismic monitoring and movement of fluids warmed by the formation to previous stimulated stages. Microseismic events follow optimal oriented fractures to the present-day stress regime and are centered significantly above the stimulated interval. The observed microseismic events may be the expression of the stress on overlying layers imposed by the injection of more than 250 cubic feet of sand and fluid per foot of lateral.

Subsequently, we evaluated the proposed attributes to see the relationship between frequency content, energy attribute, and the temperature rise for the stage 10. Figure 16 shows that the temperature rise is associated with low dominant frequency and instantaneous frequency in stage 9 while stimulation of stage 10. We suggest that a frequency damping effect is happening around the fiber. Because of the back-circulating of the gasy fluid toward the well, the fiber vibration is affected by the fluid presence and higher frequency vibrations are dampened. It results in low frequency zone in stage 9 which also shows abnormal temperature. Neither the energy attribute nor the instantaneous amplitude attribute show these abnormal zones associated with high temperature. One more explanation could be the fractures (both natural fractures and tensile fractures from stage 9 stimulation) that dampen the vibrations. As an analogy, a highly fractured rock vibrates in lower frequencies than a pristine piece of rock. However, this explanation can not justify high frequency zones in stage 9. If it was only fractures responsible for the low frequencies, there would be low frequency zones for the entire stimulation job (Figure 16). There might be contribution from both fluid and fractures in dampening the high frequencies.

We also notice that there is frequency drop when there is proppant concentration drop, it might be due to the proppants that hinder the fluid flow communication between the stages. A drop in the proppant concentration entails more hydraulic connections between the two stages and an abnormal temperature rise and a frequency attenuation. On the other hand, stage 18 stimulation does not significantly raise the temperature or create a low frequency zone in stage 17 (Figure 17).

Wireline image logs show less fracture intensity at the base of the stage 18 and top of the stage 17 than base of the stage 10 and top of the stage 9, respectively.

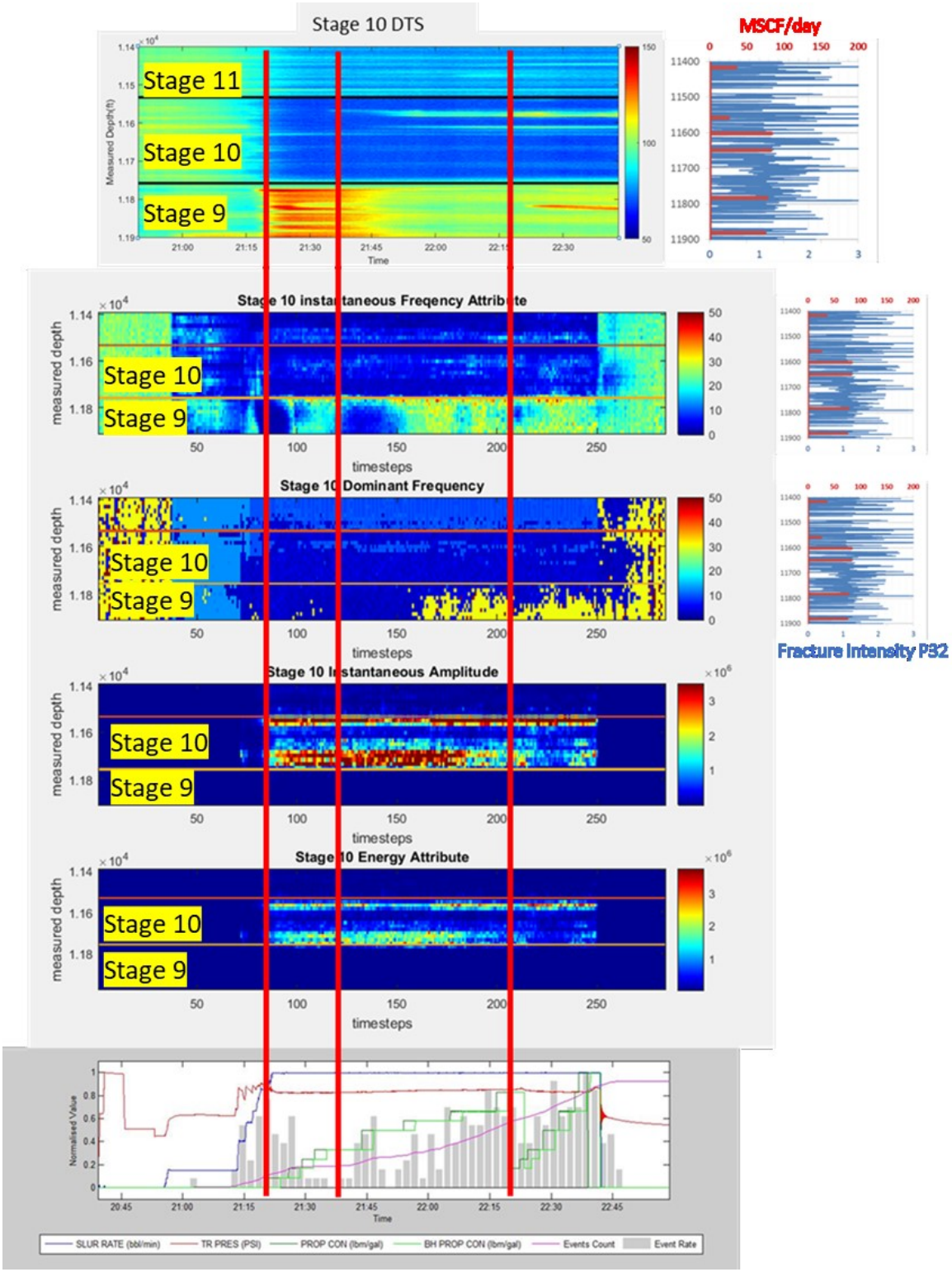

Figure 19: DTS data and stimulation parameters are compared with energy, instantaneous frequency, instantaneous amplitude, and dominant frequency. Low frequency zones are observed when there is a temperature rise in stage 9. Note that the proppant drop also creates low frequency zones in stage 9.

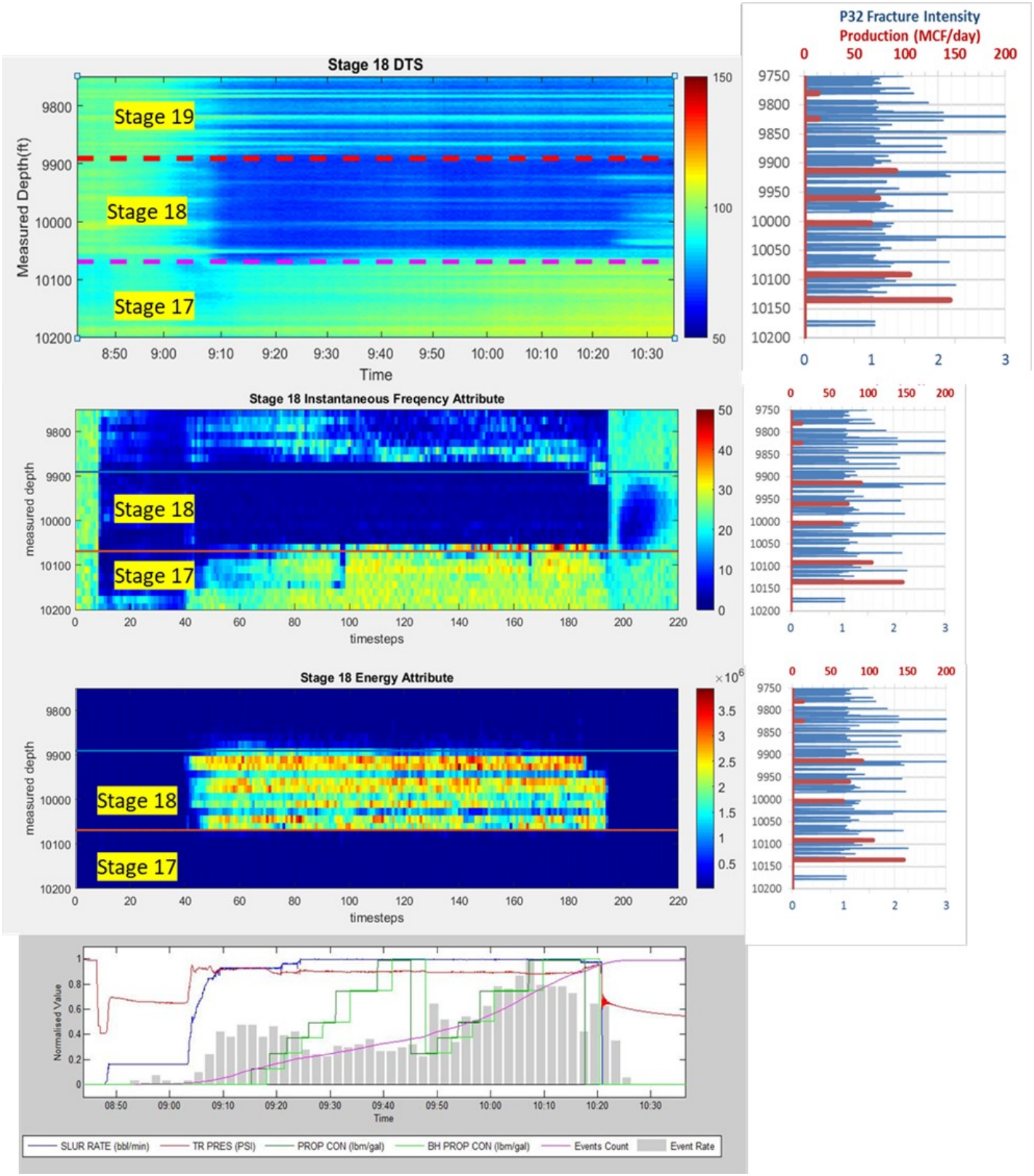

Figure 20: DTS data and stimulation parameters are compared with energy, instantaneous frequency, instantaneous amplitude, and dominant frequency. Neither the temperature rise nor the low frequency zones are significant in stage17 while stage 18 Stimulation.

Conclusions

1- Frequency attribute has been shown to be valuable tool to extract subtle spectrum variations of the DAS signals.
2- Instantaneous frequency can be calculated for each of the 60,000 samples of 493 traces in every SEGY file. However, this computation requires a considerably powerful workstation for stage of 200-300 SEGY files; in addition, the waterfall plot for 835,000,000 samples is not very easy to understand. Our results show that a temporal window of 30 seconds would make the calculations faster and generates a smoother image to visualize.
3- Although energy attribute calculation is computationally cheaper than frequency attributes, it does not show any abnormal energy variations in stage 9 while stimulation of the stage 10.
4- The temperature rise was attributed to the hydraulic connection between the stage 9 and stage 10. This connection is probably intensified by natural fractures oriented obliquely to the lateral in the reservoir.
5- Stage 18 stimulation does not cause a temperature rise in the stage 17. Instantaneous frequency also does not show a significant frequency drop in DAS response for the stage 17. This behavior is attributed to the low natural fracture intensity P32 at the base and top of the stage 18 and 17, respectively.
6- We also noticed low frequency zone in stage 9 when the proppant concentration was dropped during stage 10 stimulation. One possible explanation could be that high proppant concentration hinders the fluid communications between stage 9 and 10.
7- The less critically oriented N81°E natural fractures in the stress field seem to intensify the cross-stage flow communications. These fractures undergo slow slip and did not show significant microseismic expressions. However, more than 1500 of these fractures were observed in the wireline image logs.

Future Work

One might try an adaptive moving temporal window that has variable size in different locations of the DAS traces. For example, the smaller window size could be utilized near the top and bottom of the stimulated stages to catch more details of the frequency spectrum while a larger window could be employed for places in the middle of the stimulated stages. Other seismic attributes can be tested for the fiber optic data. The similarity attribute would be a proposed attribute to be tested for traces around the boundary of the stimulated stages.

Acknowledgement

This research is funded through the U.S.DOE National Energy Technology Lab part of their Marcellus Shale Energy and Environmental Laboratory (MSEEL) (DOE Award No.: DE-FE0024297).

We appreciate the Northeast Natural Energy LLC. For providing data and technical support.

References

Ajayi, B. T., Walker, K. J., Wutherich, K., & Sink, J. (2011, January 1). Channel Hydraulic Fracturing and Its Applicability in the Marcellus Shale. Society of Petroleum Engineers. doi:10.2118/149426-MS.

Alciatore, D.G., 2007. *Introduction to mechatronics and measurement systems*. Tata McGraw-Hill Education.

Amini, S., Kavousi, P. and Carr, T.R., 2017. Application of Fiber-optic Temperature Data Analysis in Hydraulic Fracturing Evaluation--A Case Study in Marcellus Shale. Unconventional Resources Technology Conference (URTEC).

Bakku, S.K., Fehler, M. and Wills, P., 2014. Monitoring hydraulic fracturing using distributed acoustic sensing in a treatment well. In *SEG Technical Program Expanded Abstracts 2014* (pp. 5003-5008). Society of Exploration Geophysicists.

Barnes, A.E., 1990. Analysis of temporal variations in average frequency and amplitude of COCORP deep seismic reflection data. In *SEG Technical Program Expanded Abstracts 1990* (pp. 1553-1556). Society of Exploration Geophysicists.

Barnes, A.E., 1991. Instantaneous frequency and amplitude at the envelope peak of a constant-phase wavelet. *Geophysics*, *56*(7), pp.1058-1060.

Barnes, A.E., 1992. Another look at NMO stretch. *Geophysics*, *57*(5), pp.749-751.

Barnes, A.E., 1993. Instantaneous spectral bandwidth and dominant frequency with applications to seismic reflection data. *Geophysics*, *58*(3), pp.419-428.

Barnes, A.E., 1998. The complex seismic trace made simple. *The Leading Edge*, *17*(4), pp.473-473.

Beckwith, R. (2013, June 1). The Marcellus Shale Gas Boom Evolves. Society of Petroleum Engineers. doi:10.2118/0613-0034-JPT.

Berkout, A.J., 1984. Seismic resolution: Resolving power of acoustical echo techniques. *Handbook of Geophysical Exploration, Section I, Seismic Exploration, Geophysical Press, London*, pp.181-192.

Bodine, J.H., 1984. Waveform analysis with seismic attributes. In *SEG Technical Program Expanded Abstracts 1984* (pp. 505-509). Society of Exploration Geophysicists.

Boone*, K., Crickmore, R., Werdeg, Z., Laing, C. and Molenaar, M., 2015, July. Monitoring hydraulic fracturing operations using fiber-optic distributed acoustic sensing. In *Unconventional Resources Technology Conference, San Antonio, Texas, 20-22 July 2015* (pp. 316-322). Society of Exploration Geophysicists, American Association of Petroleum Geologists, Society of Petroleum Engineers.

Carr, T.R., Wilson, T.H., Kavousi, P., Amini, S., Sharma, S., Hewitt, J., Costello, I., Carney, B.J., Jordon, E., Yates, M. and MacPhail, K., 2017. Insights from the Marcellus Shale Energy and Environment Laboratory (MSEEL). Unconventional Resources Technology Conference (URTEC).

Carr, T.R., Wang, G., Boyce, M.L. and Yanni, A., 2011, March. Understanding controls on deposition of organic content in the Middle Devonian organic-rich shale intervals of West Virginia and western Pennsylvania. In Geological Society of America Abstracts with Programs: Northeast (46th Annual) and North-Central (45th Annual) Joint Meeting, Pittsburgh (Vol. 43, No. 1, p. 50).

Carr, T.R., Wang, G. and McClain, T., 2013, March. Petrophysical analysis and sequence stratigraphy of the Utica shale and Marcellus shale, Appalachian Basin, USA. In IPTC 2013: International Petroleum Technology Conference.

Carnahan, B.D., Clanton, R.W., Koehler, K.D., Harkins, G.O. and Williams, G.R., 1999, January. Fiber Optic Temperature Monitoring Technology. In *SPE Western Regional Meeting*. Society of Petroleum Engineers.

Conway, C. and Mondanos, M., 2015, June. An introduction to fibre optic Intelligent Distributed Acoustic Sensing (iDAS) technology for power industry applications. In *Proceedings of the 9th International Conference on Insulated Power Cables, Versailles, France* (Vol. 2125, p. 16).

Das, I. and Zoback, M.D., 2012. Microearthquakes associated with long period, long duration seismic events during stimulation of a shale gas reservoir. In *SEG Technical Program Expanded Abstracts 2012* (pp. 1-5). Society of Exploration Geophysicists.

Economides, M. J., Notle, K. G. 2000. Schlumberger Reservoir Simulation, 3rd Edition, pp. 5-8 to 5-21.

Engelder, T. and Lash, G.G., 2008. Marcellus Shale Play‟ s Vast Resource Potential Creating Stir in Appalachia.

Ettensohn, F.R., 1985. The Catskill delta complex and the Acadian orogeny: A model. Geological Society of America Special Papers, 201, pp.39-50.

Ettensohn, F.R., Miller, M.L., Dillman, S.B., Elam, T.D., Geller, K.L., Swager, D.R., Markowitz, G., Woock, R.D. and Barron, L.S., 1988. Characterization and implications of the Devonian-Mississippian black shale sequence, eastern and central Kentucky, USA: Pycnoclines, transgression, regression, and tectonism.

Farnbach, J.S., 1975. The complex envelope in seismic signal analysis. *Bulletin of the Seismological Society of America*, *65*(4), pp.951-962.

Glasbergen, G., Yeager, V.J., Reyes, R.P. and Everett, D.M., 2010. Fluid-diversion monitoring: the key to treatment optimization. *SPE Production & Operations*, *25*(03), pp.262-274.

Ha, S.T.T., Sheriff, R.E. and Gardner, G.H.F., 1991. Instantaneous frequency, spectral centroid, and even wavelets. *Geophysical Research Letters*, *18*(8), pp.1389-1392.

Hardage, B., 2010. GC Instantaneous Seismic Attributes Calculated by the Hilbert Transform. Search and Discovery Article #40564.

Holley, E. and Kalia, N., 2015. Fiber-optic Monitoring: Stimulation Results from Unconventional Reservoirs. Unconventional Resources Technology Conference (URTEC).

Kallweit, R.S. and Wood, L.C., 1982. The limits of resolution of zero-phase wavelets. *Geophysics*, *47*(7), pp.1035-1046.

Karaman, O.S., Kutlik, R.L. and Kluth, E.L., 1996, January. A field trial to test fiber optic sensors for downhole temperature and pressure measurements, West Coalinga Field, California. In *SPE Western Regional Meeting*. Society of Petroleum Engineers.

Kavousi, P., Carr, T., Wilson, T., Amini, S., Wilson, C., Thomas, M., MacPhail, K., Crandall, D., Carney, B.J., Costello, I. and Hewitt, J., 2017. Correlating distributed acoustic sensing (DAS) to natural fracture intensity for the Marcellus Shale. In *SEG Technical Program Expanded Abstracts 2017* (pp. 5386-5390). Society of Exploration Geophysicists.

Kimbell, J., 2013. *History and Analysis of Distributed Acoustic Sensing (DAS) for Oilfield Applications* (Doctoral dissertation).

Kugler, I., Olmstead, R. 2015. North America Supply Analytics: Pennsylvania Marcellus.

Lash, G.G. and Engelder, T., 2011. Thickness trends and sequence stratigraphy of the Middle Devonian Marcellus Formation, Appalachian Basin: Implications for Acadian foreland basin evolution. AAPG bulletin, 95(1), pp.61-103.

Li, M., Wang, H. and Tao, G., 2015. Current and future applications of distributed acoustic sensing as a new reservoir geophysics tool. *Open Petroleum Engineering Journal*, *8*(1), pp.272-281.

MacPhail, W.F., Lisoway, B. and Banks, K., 2012, January. Fiber optic distributed acoustic sensing of multiple fractures in a horizontal well. In *SPE Hydraulic Fracturing Technology Conference*. Society of Petroleum Engineers.

Madsen, K.N., Thompson, M., Parker, T. and Finfer, D., 2013. A VSP field trial using distributed acoustic sensing in a producing well in the North Sea. *First Break*, *31*(11), pp.51-56.

Mateeva, A., Mestayer, J., Cox, B., Kiyashchenko, D., Wills, P., Lopez, J., Grandi, S., Hornman, K., Lumens, P., Franzen, A. and Hill, D., 2012. Advances in distributed acoustic sensing (DAS) for VSP. In *SEG Technical Program Expanded Abstracts 2012* (pp. 1-5). Society of Exploration Geophysicists.

Mateeva, A., Mestayer, J., Yang, Z., Lopez, J., Wills, P., Roy, J. and Bown, T., 2013. Dual-well 3D VSP in deepwater made possible by DAS. In *SEG Technical Program Expanded Abstracts 2013* (pp. 5062-5066). Society of Exploration Geophysicists.

Mestayer, J., Cox, B., Wills, P., Kiyashchenko, D., Lopez, J., Costello, M., Bourne, S., Ugueto, G., Lupton, R., Solano, G. and Hill, D., 2011. Field trials of distributed acoustic sensing for geophysical monitoring. In *SEG Technical Program Expanded Abstracts 2011* (pp. 4253-4257). Society of Exploration Geophysicists.

Miller, D., Parker, T., Kashikar, S., Todorov, M. and Bostick, T., 2012. Vertical seismic profiling using a fiber-optic cable as a distributed acoustic sensor: 74th EAGE Conference and Exhibition. In *Expanded Abstracts*.

Milliken, K.L., Rudnicki, M., Awwiller, D.N. and Zhang, T., 2013. Organic matter–hosted pore system, Marcellus formation (Devonian), Pennsylvania. AAPG bulletin, 97(2), pp.177-200.

Molenaar, M.M. and Cox, B.E., 2013, January. Field cases of hydraulic fracture stimulation diagnostics using fiber optic distributed acoustic sensing (DAS) measurements and Analyses. In *SPE Unconventional Gas Conference and Exhibition*. Society of Petroleum Engineers.

Molenaar, M.M., Hill, D., Webster, P., Fidan, E. and Birch, B., 2012. First downhole application of distributed acoustic sensing for hydraulic-fracturing monitoring and diagnostics. *SPE Drilling & Completion*, *27*(01), pp.32-38.

OpendTect Documentaion at:
http://doc.opendtect.org/5.0.0/doc/od_userdoc/content/app_a/freq.htm

Parker, T., Shatalin, S. and Farhadiroushan, M., 2014. Distributed Acoustic Sensing–a new tool for seismic applications. *First Break*, *32*(2), pp.61-69.

Rahman, M., Zannitto, P.J., Reed, D.A. and Allan, M.E., 2011, January. Application of fiber-optic distributed temperature sensing technology for monitoring injection profile in belridge field, diatomite reservoir. In *SPE Digital Energy Conference and Exhibition*. Society of Petroleum Engineers.

Rao, M. and Qiu, H., 1993. Process Control Engineering: A Textbook for Chemical, Mechanical, and Electrical Engineering, Vol. 1. *Gordon and Breach Science, New York, NY, USA*.

Robertson, J.D. and Nogami, H.H., 1984. Complex seismic trace analysis of thin beds. *Geophysics*, *49*(4), pp.344-352.

Robertson, J.D. and Fisher, D.A., 1988. Complex seismic trace attributes. *The Leading Edge*, *7*(6), pp.22-26.

Shelley, R., Nejad, A., Guliyev, N., Raleigh, M., & Matz, D. (2014, October 21). Understanding Multi-Fractured Horizontal Marcellus Completions. Society of Petroleum Engineers. doi:10.2118/171003-MS

Sheriff, R.E. and Geldart, L.P., 1995. *Exploration seismology*. Cambridge university press.

Sheriff, R.E., Taner, M.T., Koehler, F. and Frye, D., 1977. Extraction and interpretation of the complex seismic trace.

Sierra, J.R., Kaura, J.D., Gualtieri, D., Glasbergen, G., Sarker, D. and Johnson, D., 2008, January. DTS monitoring of hydraulic fracturing: experiences and lessons learned. In *SPE Annual Technical Conference and Exhibition*. Society of Petroleum Engineers.

Song, L., Paronish, T., Agrawal, V., Hupp, B., Sharma, S. and Carr, T.R., 2017. Depositional Environment and Impact on Pore Structure and Gas Storage Potential of Middle Devonian Organic Rich Shale, Northeastern West Virginia, Appalachian Basin. Unconventional Resources Technology Conference (URTEC).

Tai, S., 2009. *Analysis of frequency characteristics of seismic reflections with attenuation in thin layer zone: Methods and applications*. University of Houston.

Taner, M.T. and Sheriff, R.E., 1977. Application of amplitude, frequency, and other attributes to stratigraphic and hydrocarbon determination: section 2. Application of seismic reflection configuration to stratigraphic interpretation.

Taner, M.T., Koehler, F. and Sheriff, R.E., 1979. Complex seismic trace analysis. *Geophysics*, *44*(6), pp.1041-1063.

Tanimola, F. and Hill, D., 2009. Distributed fibre optic sensors for pipeline protection. *Journal of Natural Gas Science and Engineering*, *1*(4), pp.134-143.

Walker, K. J., Wutherich, K., Terry, I., Shreves, J. E., & Caplan, J. (2012, January 1). Improving Production in the Marcellus Shale Using an Engineered Completion Design: A Case Study. Society of Petroleum Engineers. doi:10.2118/159666-MS.

Wang, G. and Carr, T.R., 2013. Organic-rich Marcellus Shale lithofacies modeling and distribution pattern analysis in the Appalachian Basin. AAPG bulletin, 97(12), pp.2173-2205.

Webster, P., Wall, J., Perkins, C. and Molenaar, M., 2013. Micro-Seismic detection using distributed acoustic sensing. In *SEG Technical Program Expanded Abstracts 2013* (pp. 2459-2463). Society of Exploration Geophysicists.

White, R.E., 1991. Properties of instantaneous seismic attributes. *The Leading Edge*, *10*(7), pp.26-32.

Widess, M.B., 1982. Quantifying resolving power of seismic systems. *Geophysics*, *47*(8), pp.1160-1173.

Wilson, T., Carr, T., Carney, B.J., Hewitt, J., Costello, I., Jordon, E., MacPhail, K., Uschner, N., Thomas, M., Akin, S. and Magbagbeola, O., 2016. Microseismic and model stimulation of natural fracture networks in the Marcellus Shale, West Virginia. In *SEG Technical Program Expanded Abstracts 2016* (pp. 3088-3092). Society of Exploration Geophysicists.

Yilmaz, O., 1987. Seismic Data Processing: Society of Exploration Geophysiscists.

Zagorski, W.A., Wrightstone, G.R. and Bowman, D.C., 2012. The Appalachian Basin Marcellus gas play: Its history of development, geologic controls on production, and future potential as a world-class reservoir.

Zhang, J.J. and Bentley, L.R., 2000. Complex seismic trace analysis and its application to time-lapse seismic surveys. *CREWES, Geology and Geophysics, University of Calgary*.

Cost Status

Year 1

Start: 10/01/2014 End: 09/30/2017

Baseline Reporting Quarter

	Q1 (12/31/14)	Q2 (3/30/15)	Q3 (6/30/15)	Q4 (9/30/15)
Baseline Cost Plan	(From 424A, Sec. D)			
(from SF-424A)				
Federal Share	$549,000		$3,549,000	
Non-Federal Share	$0.00		$0.00	
Total Planned (Federal and Non-Federal)	$549,000		$3,549,000	
Cumulative Baseline Costs				
Actual Incurred Costs				
Federal Share	$0.00	$14,760.39	$237,451.36	$300,925.66
Non-Federal Share	$0.00	$0.00	$0.00	$0.00
Total Incurred Costs - Quarterly (Federal and Non-Federal)	$0.00	$14,760.39	$237,451.36	$300,925.66
Cumulative Incurred Costs	$0.00	$14,760.39	$252,211.75	$553,137.41
Uncosted				
Federal Share	$549,000	$534,239.61	$3,296,788.25	$2,995,862.59
Non-Federal Share	$0.00	$0.00	$2,814,930.00	$2,814,930.00
Total Uncosted - Quarterly (Federal and Non-Federal)	$549,000	$534,239.61	$6,111,718.25	$5,810,792.59

Start: 10/01/2014 End: 09/30/2017

Baseline Reporting Quarter

	Q5 (12/31/15)	Q6 (3/30/16)	Q7 (6/30/16)	Q8 (9/30/16)
Baseline Cost Plan	(From 424A, Sec. D)			
(from SF-424A)				
Federal Share	$6,247,367		$7,297,926	
Non-Federal Share	2,814,930		$4,342,480	
Total Planned (Federal and Non-Federal)	$9,062,297	$9,062,297.00	$11,640,406	
Cumulative Baseline Costs				
Actual Incurred Costs				
Federal Share	$577,065.91	$4,480,939.42	$845,967.23	$556,511.68
Non-Federal Share	$0.00	$2,189,863.30	$2,154,120.23	$0.00
Total Incurred Costs - Quarterly (Federal and Non-Federal)	$577,065.91	$6,670,802.72	$3,000,087.46	$556,551.68
Cumulative Incurred Costs	$1,130,203.32	$7,801,006.04	$10,637,732.23	$11,194,243.91
Uncosted				
Federal Share	$5,117,163.68	$636,224.26	$1,004,177.30	$447,665.62
Non-Federal Share	$2,814,930.00	$625,066.70	($1,503.53)	($1,503.53)
Total Uncosted - Quarterly (Federal and Non-Federal)	$2,418,796.68	$1,261,290.96	$1,002,673.77	$446,162.09

Start: 10/01/2014 End: 09/30/2017

Baseline Reporting Quarter	Q9 (12/31/16)	Q10 (3/30/17)	Q11 (6/30/17)	Q12 (9/30/17)
Baseline Cost Plan	(From 424A, Sec. D)			
(from SF-424A)				
Federal Share				$9,128,731
Non-Federal Share				$4,520,922
Total Planned (Federal and Non-Federal)				$13,649,653
Cumulative Baseline Costs				
Actual Incurred Costs				
Federal Share	$113,223.71	$196,266.36	$120,801.19	$1,147,988.73
Non-Federal Share	$0.00	$0.00	$0.00	$0.00
Total Incurred Costs - Quarterly (Federal and Non-Federal)	$113,223.71	$196,266.36	$120,801.19	$1,147,988.73
Cumulative Incurred Costs	$11,307,467.62	$11,503,733.98	$11,624535.17	$12,772,523.90
Uncosted				
Federal Share	$334,441.91	$138,175.55	$17,374.36	$700,190.63
Non-Federal Share	($1,503.53)	($1,503.53)	($1,503.53)	$176,938.47
Total Uncosted - Quarterly (Federal and Non-Federal)	$332,938.38	$136,672.02	$15,870.83	$877,129.10

Start: 10/01/2014 End: 09/30/2017

Baseline Reporting Quarter	Q13 (12/31/17)	Q14 (3/30/18)	Q15 (6/30/18)	Q15 (9/30/18)
Baseline Cost Plan	(From 424A, Sec. D)			
(from SF-424A)				
Federal Share				
Non-Federal Share				
Total Planned (Federal and Non-Federal)				
Cumulative Baseline Costs				
Actual Incurred Costs				
Federal Share	$112,075.89			
Non-Federal Share	$0.00			
Total Incurred Costs - Quarterly (Federal and Non-Federal)	$112,075.89			
Cumulative Incurred Costs	$12,884,599.79			
Uncosted				
Federal Share	$588,114.74			
Non-Federal Share	$176,938.47			
Total Uncosted - Quarterly (Federal and Non-Federal)	$765,053.21			

National Energy Technology Laboratory

626 Cochrans Mill Road
P.O. Box 10940
Pittsburgh, PA 15236-0940

3610 Collins Ferry Road
P.O. Box 880
Morgantown, WV 26507-0880

13131 Dairy Ashford Road, Suite 225
Sugar Land, TX 77478

1450 Queen Avenue SW
Albany, OR 97321-2198

Arctic Energy Office
420 L Street, Suite 305
Anchorage, AK 99501

Visit the NETL website at:
www.netl.doe.gov

Customer Service Line:
1-800-553-7681